

UNIVERSITY OF PADERBORN

FACULTY OF SCIENCE

DISSERTATION

**Influence of spin-orbit coupling
on the electronic structure of
low-dimensional systems**

Nora Jenny Vollmers

Eine Dissertation

zur Erlangung des akademischen Grades

Doktor der Naturwissenschaften (Dr. rer. nat.)

vorgelegt dem

Department Physik der Fakultät für Naturwissenschaften

Universität Paderborn.

2016

I'm not sure. I'm afraid we need to use... math!

— Professor Hubert J. Farnsworth [1]

Abstract

The search for new techniques, materials and ideas to improve and develop high efficient electrical devices is more relevant today as ever. In this doctorate thesis *ab-initio* density functional theory (DFT) is used to investigate two very different systems with very different properties. They have in common that they are low-dimensional (1D and 2D) and that spin-orbit coupling (SOC) is necessary for an accurate description. Therefore, at the beginning of this these, a new, high efficient relativistic approach is introduced which allows for an inclusion of SOC without pushing the computational limits.

The first explored system is given by indium-nanowires that self-organize on the silicon (111) surface. This quasi one-dimensional system is famous for its reversible temperature-induced phase transition from a (4×1) to a (8×2) structure. Although most properties are already studied intensively, the inclusion of SOC in the calculations unfolds a so far unknown but large Rashba splitting, located at the In-related bands, for both phases which is strongly anisotropic.

The second material investigated in this work is the bismuth (111) surface. The clean surface is a challenge itself as its electronic structure highly depends on the correct modelling. In contrast to the In-nanowires where most properties can be described without SOC, it is essential in the case of bismuth. Dramatic alterations in the band structure and Fermi surface are clearly the most obvious changes. The bismuth surface has spin-split surface states, a precondition for spintronics but a good understanding of controlled surface modification is useful for future applications. It is shown that transition metals (TMs) as well as noble metals occupy all the same sevenfold coordinated position within the first bismuth bilayer of the Bi(111) surface. Interestingly, the surface topography is unchanged. For the $3d$ TMs this incorporation even happens *barrier-free*, i.e. without thermal activation. By increasing the density of the adatoms, it is possible to create an energetically very stable δ -doping layer of $3d$ TMs which, while being invisible to scanning tunneling microscopy (STM), leads to changes of the electronic and magnetic surface properties.

Kurzfassung

Die Suche nach neuen Techniken, Materialien und Ideen um hocheffiziente elektronische Bauelemente zu verbessern und zu entwickeln ist heute aktueller denn je. In dieser Doktorarbeit wird *ab-initio* Dichtefunktionaltheorie (DFT) genutzt um zwei sehr verschiedene Systeme mit sehr unterschiedlichen Eigenschaften zu untersuchen. Beiden ist gemein, dass sie von niedriger Dimension (2D und 3D) sind und dass Spin-Bahn-Kopplung (SOC) notwendig für eine akkurate Beschreibung ist. Daher wird zu Beginn dieser Dissertation ein neuer, effizienter relativistischer Ansatz eingeführt, mit dem die SOC berücksichtigt wird ohne die Grenzen der Rechenleistung zu sprengen.

Bei dem ersten untersuchten System handelt es sich um Indium Nanodrähte, die sich selbstorganisierend auf der Silizium (111) Oberfläche anordnen. Dieses quasi-eindimensionale System ist bekannt für seinen reversiblen temperaturinduzierten Phasenübergang von einer (4×1) zu einer (8×2) Struktur. Obwohl die meisten Eigenschaften bereits umfassend untersucht wurden, zeigt die Integration von SOC eine bisher unbekannte, aber große anisotrope Rashba-Aufspaltung für beide Phasen, lokalisiert an den In-Bändern.

Das zweite in dieser Arbeit untersuchte Materialsystem ist die Bismut (111) Oberfläche. Die reine Oberfläche ist schon selbst eine Herausforderung, da die elektronische Struktur stark an der korrekten Modellierung hängt. Im Gegensatz zu den In-Nanodrähten, wo die meisten Eigenschaften ohne SOC beschrieben werden können, ist sie essentiell im Falle von Bismut. Große Veränderungen in der Bandstruktur und Fermifläche sind deutlich sichtbar. Die Bismut Oberfläche besitzt spin-aufgespaltene Oberflächenzustände, eine Voraussetzung für Spintronik. Dennoch ist ein gutes Verständnis von kontrollierter Modifikation der Oberfläche nützlich für zukünftige Anwendungen. Wir zeigen, dass Übergangsmetalle (TM) sowie Edelmetalle dieselbe siebenfach koordinierte Position innerhalb der ersten Bismut Bilage der Bi(111) Oberfläche besetzen. Interessanterweise wird hierbei die Oberflächentopographie nicht verändert. Für die $3d$ TMs geschieht dieser Einbau sogar *barrierefrei*, d.h. ohne thermische Aktivierung. Durch Erhöhung der Adatomdichte ist es möglich eine δ -dotierende Lage von $3d$ TMs zu kreieren, welche, obwohl unsichtbar für STM Messungen, zu Änderungen der elektronischen und magnetischen Oberflächeneigenschaften führt.

Acknowledgements

An erster Stelle gilt mein Dank Dr. Uwe Gerstmann. Seine überragende Betreuung während meiner gesamten Promotionszeit hat diese Arbeit erst möglich gemacht. Dann möchte ich besonders Prof. Dr. Wolf Gero Schmidt danken, der mir die Möglichkeit zur Promotion gegeben hat. Er stand mir bei jedem Problem (ob wissenschaftlicher oder anderer Natur) immer mit Rat und Tat zur Seite. Auch danke ich ihm dafür, dass er es mir ermöglicht hat, Konferenzen in der gesamten Welt zu besuchen. Dadurch konnte ich sowohl persönlich als auch wissenschaftlich meinen Horizont erweitern.

Der gesamten Arbeitsgruppe, aber auch speziell Büro N3.301, möchte ich für die gemeinsame Zeit, die tolle Arbeitsatmosphäre und den vielen Diskussionen rund um Physik und die Welt danken.

Danke an Claudius Klein und Prof. Dr. Horn-von Hoegen von der Universität Duisburg-Essen, sowie Prof. Dr. Tegenkamp, Prof. Dr. Pfnür und Philipp Kröger von der Leibniz Universität Hannover für die tolle Zusammenarbeit. Die Kombination aus experimenteller und theoretischer Anschauung war für mein Verständnis der vorliegenden Arbeit sehr hilfreich.

Vielen Dank auch an meine Familie, an die Doppelkopfrunde, an die Skifahrerfreunde und an das literarischen Quintett für die schönen Stunden, die wir zusammen verbringen konnten. Ihr habt mir jederzeit gezeigt, dass das Leben nicht nur aus Promotion besteht.

Abschließend möchte ich meinem Ehemann Jan Milan Eyni für seine ausdauernde und liebevolle Unterstützung danken.

Contents

Abstract	1
Acknowledgements	5
Contents	7
List of Figures	9
List of Tables	11
List of Symbols	13
1 Introduction	15
2 A kind of theoretical background	19
2.1 Describing solids – the long way to quantum mechanics	19
2.2 Density functional theory – Efficiency	22
2.3 Relativistic quantum mechanics	24
3 In/Si(111) nanowires	31
3.1 Crystal structure and modelling	32
3.2 Rashba splitting	33
4 The bismuth (111) surface	41
4.1 The Bi(111) surface	42
4.1.1 Technical details	42
4.1.2 Crystal structure	43
4.1.3 Modeling of the surface	45
4.2 Adatom incorporation into the Bi(111) surface	54
4.2.1 Experiment	55
4.2.2 DFT calculations	58
4.2.3 <i>Barrier-free</i> subsurface incorporation of isolated 3 <i>d</i> metal atoms into Bi(111) films	59
4.2.4 Bi(111) surface δ -doping by transition metal atoms	63

Contents

5 Summary	71
6 Outlook	75
Bibliography	79

List of Figures

1.1	Datta-Das spin field-effect transistor	16
1.2	InAs nanowire field-effect transistor	16
2.1	Schematic view of the Bi(111) bilayer	26
2.2	Band structure of a single Bi bilayer calculated with different types of approaches	27
3.1	Schematic view of the In/Si(111) (4×1) and (8×2) model	32
3.2	Scalar-relativistic and full-relativistic band structures calculated for the In/Si(111) (4×1) and (8×2) phase	34
3.3	3 <i>d</i> band structure	35
3.4	Visualization of the orbital character of the In-related bands for the In/Si(111) (4×1) and (8×2) phase	37
4.1	Bismuth crystal	41
4.2	Bismuth bulk band structure	43
4.4	Schematic view of the clean Bi(111) surface	44
4.3	Bismuth bulk unit cell	44
4.5	Band structures of Bi(111) films	46
4.6	Band structures of the clean bismuth (111) surface for symmetric slabs with different numbers of bilayers.	49
4.7	2D plot of the Fermi surface for the clean Bi(111) surface.	50
4.8	Band structure of a symmetric ten bilayer Bi(111) with different numbers of fixed bilayers	51
4.9	Band structure of a symmetric δ -doped Bi(111) surface.	52
4.10	2D plot of the Fermi surfaces for the δ -doped Bi(111) surface.	53
4.11	experimental STM image of impurity atoms deposited on the Bi(111) surface	56
4.12	experimental STM image of Bi(111)	57
4.13	positions of the STM pattern from the experimental STM image of the Bi(111) surface	58
4.14	total energy curve for adatom positions in the Bi(111) surface	59
4.15	Schematic view of Co in Bi(111)	60
4.16	Calculated STM image for minimum I and minimum II	61
4.17	Binding energies for different Co arrangements	64
4.18	Schematic view of δ -doping Co layer in Bi(111)	65
4.19	Relativistic bandstructure of the Co/Bi(111) surface	66

4.20	2D plot of the Fermi surfaces for the clean and the δ -doped Bi(111) surface.	67
4.21	Experimental and calculated STM images for different arrangements of subsorbates	67
4.22	Comparison of the calculated STM pictures for the clean and the δ -doped Bi(111) surface	68
4.23	Side view of Co at the Bi(111) surface and possible arrangements of Co atoms	69
6.1	XMCD of bcc-Fe resolved into the different contributions.	77

List of Tables

2.1	Energy gap in meV for graphene calculated with different methods and pseudopotentials.	28
2.2	Rashba parameters of Bi-related surface alloys, calculated with different approaches and compared with experimental results and former all-electron DFT calculations.	29
3.1	Rashba parameter for the In/Si(111) (4×1) and (8×2) phase compared to literature.	36
3.2	Contributions of p orbitals to the In surface bands	37
4.1	Calculated adsorption and incorporation energies for different atomic species at the Bi(111) surface	62

List of Symbols

$\hat{\mathcal{H}}$	Hamiltonian of Schrödinger's equation
$\Psi(\mathbf{r}, t)$	wave function of a single particle at position \mathbf{r} and time t
$\Psi(\{\mathbf{r}_j\}, \{\mathbf{R}_n\})$	wave function of a system of electrons with coordinates $\{\mathbf{r}_j\}$ and nuclei with coordinates $\{\mathbf{R}_n\}$
$n(\mathbf{r})$	electron density
$\delta(\mathbf{r} - \mathbf{r}_i)$	Dirac-Delta function
$E[n(\mathbf{r})]$	energy functional of the electron density $n(\mathbf{r})$
$E_0 = E[n_0]$	energy functional of the ground state energy n_0
$T_s[n(\mathbf{r})]$	kinetic energy of non-interacting particles
$v(\mathbf{r})$	external potential arising from the nuclei
$E_{xc}[n(\mathbf{r})]$	exchange correlation functional including all unknown many-body effects
$\phi_l(\mathbf{r})$	non-interacting single-particle orbitals
ϵ_l	energies of the non-interacting single particle orbitals
$c = 137$	speed of light (in atomic units)
$\boldsymbol{\alpha}, \boldsymbol{\beta}$	with $\alpha_i = \begin{pmatrix} 0 & \sigma_i \\ \sigma_i & 0 \end{pmatrix}$ and $\beta = \begin{pmatrix} 1 & 0 \\ 0 & -1 \end{pmatrix}$ 4x4-matrices
$\hat{\sigma}$	Spin-Pauli matrices
\hat{p}	momentum operator
\mathbf{A}	vector potential
\mathbf{E}	electric field
\mathbf{B}	magnetic field
E_{rel}	relativistic Energy

$\hat{\mathcal{H}}_{FW}$	Foldy-Wouthuysen transformed Hamiltonian
\hat{G}	Identity operator
$\mu_B = \frac{1}{2}$	Bohr magneton (in atomic units)
$\Delta\hat{\mathcal{H}}_{SO}$	spin-orbit including part of the Hamiltonian
$\hat{\mathcal{T}}$	Blöchl's PAW transformation
$p_{r,m}$	two-component projectors set up from scalar-relativistic components
V_{ps}	pseudo potential
V_{ae}	all-electron potential
$ \psi\rangle$	all-electron spinor
$ \bar{\psi}\rangle$	pseudospinor
$\hat{\mathcal{L}}$	angular momentum operator
$\hat{\mathcal{H}}_R$	Rashba Hamiltonian
α_R	Rashba parameter
E_R	energy splitting due to the Rashba effect
Δk	splitting in reciprocal space due to the Rashba effect
m^*	effective mass

Chapter 1

Introduction

When Gordon Moore in 1965 formulated his famous law that the number of transistors in an integrated circuit doubles approximately every two years [2], no one expected that it holds true even 50 years later. With the progress in solid-state physics and engineering it is possible to build smaller and smaller devices. Today, smartphones are equipped with devices on the scale of around 14 nm. Even though research is already reaching the atomic scale [3, 4], it is safe to say that commercial use is still far away. Even Moore himself predicts the ending of his law [5]:

“I guess I see Moore’s Law dying here in the next decade or so, but that’s not surprising.”

It is time to think about possibilities to push technological boundaries. The smaller the size, the more important quantum effects become. Although the idea of Quantum computing can be dated back to the 1970s (maybe as a reaction to Moore’s law), first realisations were made in the past years [7, 8] and culminates in GOOGLE’s publication regarding the extraordinary speed of their quantum computer [9]. Qubits can be realised in various ways and one of it is the manipulation of the electron spin. For the success of *spintronics* the understanding of the underlying physics is essential. The Stern-Gerlach experiment showed that the magnetic moment can couple to external magnetic fields [10–12]. Thus, external fields can be used to control the spin. For practical application, however, magnetic fields on the nanoscale are hard to handle. Spin-orbit coupling (SOC) can be seen as a “built-in” magnetic field. Supriyo Datta and Biswajit Das proposed a transistor based on SOC [13], cf. Figure 1.1. The Datta-Das spin field-effect transistor

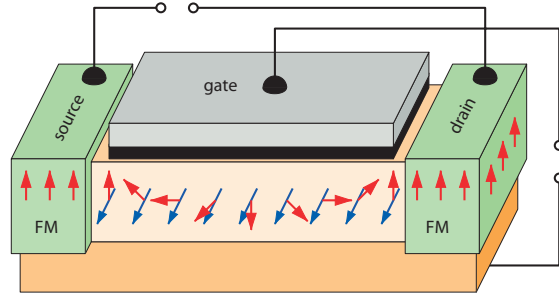


FIGURE 1.1: The Datta-Das spin field-effect transistor (SFET). The source contact on the left injects spin-polarized electrons (red arrows) into a semiconductor channel. The gate voltage controls the spin-orbit coupling (SOC) and the resulting effective magnetic field (blue arrows). The electrons' spins precess. The current depends on the angle between electron and drain magnetization. Taken from [6].

(SFET) consists of two ferromagnetic contacts (source and drain) separated by a semiconductor region, e.g a quasi-one-dimensional InGaAs/InAlAs heterojunction. The contacts act as a spin injector and spin detector. The injected electrons are spin-polarized. Due to the SOC the spin precesses during the electron's way through the semiconductor. When they reach the spin detector those electrons with their spin aligned to the drain magnetization contribute most to the current. The current depends on the angle between electron and drain magnetization and thus on the strength of the SOC. The SOC and with it the degree of spin precession is tunable by the voltage applied to the gate.

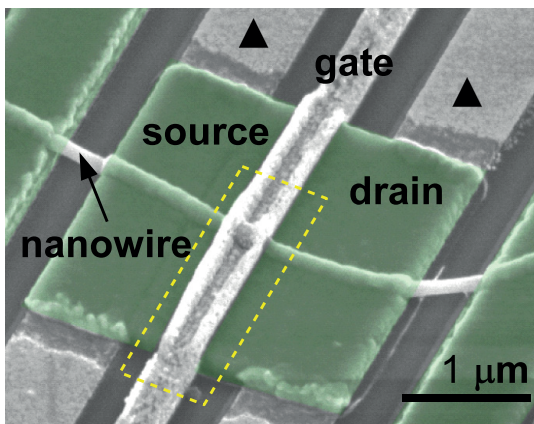


FIGURE 1.2: Scanning electron microscope (SEM) image of a fabricated InAs nanowire field-effect transistor. The source/drain contacts are Al/Al₂O₃. The gate electrodes consist of Ti/Au. Taken from [14].

Not only the use of new physics, but also the use of new material systems can be beneficial. Most of the devices today are, just like the world around us, three-dimensional. But if we go to lower dimensions, a whole new world opens before us. Surfaces can be seen as two-dimensional systems. Just like defects, they disturb the regular periodicity of a crystal and create new electronic states in the band structure. Those can lead to totally different properties. In this work bismuth is investigated. It is classified as

a semimetal when regarding the bulk crystal. At most points of the Brillouin zone

exists an energy gap like in a semiconductor, but there are points where the valence and conduction bands overlap making bismuth formally a metal. However, the surface shows several clearly visible metallic surface states making the bismuth surface a model system for a 2D-metal. Due to spin-orbit coupling, those surface state bands exhibit a strong spin splitting. This makes bismuth very valuable in the field of spintronics and quantum computing.

But, the dimensionality can be reduced even further. In one-dimensional systems electrons are confined in all but one direction. As a consequence of this, most of their properties have a highly anisotropic character, e.g. resistance and conductance. Furthermore, models developed for three-dimensional systems, are not valid anymore and new physical phenomena can be discovered. For instance, the so-called Fermi liquid model, where quasiparticles carry charge and spin character, has to be replaced by the Luttinger liquid model [15]. Here, a spin-charge separation takes place and the resulting spin-density waves (SDW) and charge-density waves (CDW) propagate with different group velocities.

Atomic-sized nanowires on a substrate are quasi one-dimensional systems and very promising candidates for future electronic nanodevices. They can act as passive interconnects – without conducting wires there are no circuits – but also as the active devices themselves. A nanowire field effect transistor is easy to imagine with the nanowire connecting the two contacts, c.f. Figure 1.2.

The presented work aims at improving the understanding of the one-dimensional In-nanowires and the two-dimensional bismuth (111) surface and the possibility of manipulation of the surface states by using *ab-initio* density functional theory (DFT). For all calculations the QUANTUM ESPRESSO [16] package was used. As open-source software it allows for a direct extension with features necessary for this work: The investigated systems contain indium and bismuth. Both elements are heavy and as our structures consist of up to 162 atoms, a computational cost saving handling of SOC is needed.

At the beginning, we present the theoretical background and establish a new efficient approach to include relativistic effects in the calculations. Chapter 3 deals with In-nanowires which self-organize on the silicon (111) and deem as a prototype for a one-dimensional nanowire. The inclusion of relativistic treatment in our calculations reveals a large, strongly anisotropic Rashba splitting of the In-related states. Afterwards, in Chapter 4, we change the system and go to the two-dimensional bismuth (111) surface. At first, we determine the best way to model the surface before we investigate the influence of adatoms. Experiments

already indicated a subsurface incorporation of $3d$ transition metals (TMs) and noble metals. In fact, our calculations reveal that they are incorporated at a highly symmetric position within the uppermost bilayer of the surface. This incorporation occurs even *barrier-free* for the $3d$ TMs. A high density of those subsorbates finally leads to an energetically very stable δ -doping layer of $3d$ metals which results in changes of the surface electronic density of states and the surface magnetic properties.

Chapter 2

A kind of theoretical background

Most of the theoretical background needed for this work can be found in different textbooks [17]. Hence, we just want to give a small overview by summarizing the history of solid-state physics and quantum mechanics. Since this is a physicist's and not a historian's thesis, not everything can be covered. A good and recommended book, where most of the following chapter is based on, is *Out of the crystal maze: A history of solid state physics* by Lillian Hoddeson, Ernest Braun, Jürgen Teichmann and Spencer Weart [18].

2.1 Describing solids – the long way to quantum mechanics

Since centuries people try to understand the world around them and naturally the objects they can put in their hands, solid-state bodies. Especially during the industrial revolution in the 19th century the call for a better understanding of materials (e.g. steel) and thus efficiency enhancement was great. Successes like those of the german company Krupp which increased its steel production from 5000 tons to 50000 tons within five years can be credited to new advances in the understanding of steel [19] and helped solid-state physics to really make its breakthrough. In the 1880s the incandescent light bulb came to private households and became an intensively studied object in physics. In this context Heinrich Friedrich Weber published his paper “Untersuchungen über die Strahlung fester Körper” in 1888 where he wrote about a relation between the wavelength of light

emitted by a body and its temperature [20]. Although it did not gain a lot of attention by the time of publication, this and some other findings clearly laid the foundation for Max Planck's famous works fifteen years later [21, 22].

With new reputation and more resources it was only a matter of time that the electron was finally discovered, as it was already proposed, by Sir Joseph John Thomson at the end of the 19th century [23]. This led to a series of progression in the field of theoretical physics since the electron is essential for understanding solids on a microscopic scale.

One of the most promising theories was the one of Paul Drude [24], later modified by John Joseph Thomson [25] and Hendrik Antoon Lorentz [26]. It is derived from the kinetic gas theory and assumes that the mobile electrons and immobile ions behave like a classical gas. Drude managed for the first time to derive the Wiedemann-Franz law $\frac{\kappa}{\alpha} = \frac{4}{3} \frac{\alpha^2}{e} T$ [27] on a microscopic scale.

These "classical" theories were and still are very successful in being consistent with a lot of experiments. Unfortunately, it soon became clear that they are not enough and fail to explain for example the electron's role in the specific heat.

Even though, new theories lead to a better understanding of solids, we have already seen that the experimental side did not stand still. One of the pioneers was the theorist Max von Laue who discovered together with Walter Friedrich and Paul Knipping the diffraction of X-rays by crystals in 1912 [28]. With this technique it was possible for the first time to draw conclusions to the crystal structure of a solid. Beginning with William Henry Bragg and William Lawrence Bragg [29] the method was extended and refined more and more. Today we are able to determine the position of the atoms in various kinds of different crystals within a few percent. Besides, there were of course many other inventions indispensable today, e.g. low-temperature experiments which ultimately lead to the discovery of superconductivity by Heike Kamerlingh-Onnes [30].

Around the same time as Drude published his new theory, Max Planck derived his black-body radiation law [21, 22]. His revolutionary idea was that energy can only be emitted or adsorbed in quantized portions whose smallest unit corresponds to $\varepsilon = h\nu$ with $h = 6.626 \dots \cdot 10^{-34}$ Js being the later called Planck constant.

"It was as if the ground had been pulled out from under one, with no firm foundation to be seen anywhere upon which one could have built."

Albert Einstein’s quote from 1949 [31] displays the impact of Planck’s new theory. The great agreement between theory and experiment proved this ansatz right. Albert Einstein himself used energy quanta, photons, to explain the photoelectric effect [32]. The astonishing consequence is the particle nature for light. Hence, it is safe to say that Planck’s thoughts mark the beginning of quantum mechanics.

“Can nature possibly be so absurd as it seemed to us in these atomic experiments?”

— Werner Heisenberg 1958 [33]

Planck’s idea brought new life into physics. 1913 Nils Bohr wrote his famous paper “On the Constitution of Atoms and Molecules” where he provided an explanation for the spectral lines of hydrogen based on the works of Planck and Einstein [34]. Ten years later Louis de Broglie stated that particles can exhibit wave characteristics and waves can exhibit particle characteristics [35], another ground breaking insight.

With the ground of Planck, Einstein, Bohr, de Broglie and others a complete new theory was developed within the following years. At the beginning it was a common approach to take classical mechanics but to “quantize” certain quantities. This resulted in a lot of different quantization rules for various situations. In 1925 Werner Heisenberg, Max Born and Pascual Jordan formulated the matrix mechanics [36–38] which brought all those rules together in a, at this time, very complex and very abstract way: Matrices represent physical properties that evolve in time. In the 1920s the mathematics of matrices was not very widespread. Thus, Heisenberg’s theory did not gain the popularity it deserved. Around the same time, Erwin Schrödinger formulated an alternative approach to quantum mechanics, the so-called wave mechanics [39]. The most famous formula of this theory is with no doubt Schrödinger’s equation¹

$$i \frac{\partial}{\partial t} \Psi(\mathbf{r}, t) = \hat{\mathcal{H}} \Psi(\mathbf{r}, t) \quad (2.1)$$

or in a stationary, many-particle form

$$\hat{\mathcal{H}} \Psi(\{\mathbf{r}_j\}, \{\mathbf{R}_n\}) = E \Psi(\{\mathbf{r}_j\}, \{\mathbf{R}_n\}) \quad (2.2)$$

¹In this work atomic units are used except as noted otherwise. This means $\tilde{r} = \frac{r}{r_B}$ with $r_B = \frac{\hbar^2}{me^2}$ and $\tilde{E} = \frac{E}{E_H}$ with $E_H = \frac{\hbar^2}{2me^2}$. The tilde is neglected for better view.

Both theories, Heisenberg's matrix mechanics and Schrödinger's wave mechanics, seem very different but in fact they are totally equivalent as proven by Schrödinger himself [40] and American physicist Carl Eckart [41]. It should be noted that there exists a third formulation of quantum mechanics. Richard Feynman, build on the work of Paul Dirac [42, 43], developed the path-integral formulation of quantum mechanics [44]. Here, all possible paths of a motion of a particle are taken into consideration and not just the path with the stationary action as it is the case in Hamilton's principle. The different paths have different weights. The path integral, or functional integral, over those paths results in a so-called quantum or probability amplitude.

2.2 Density functional theory – Efficiency

Schrödinger's equation in the presented form (Eq. (2.2)) fully describes a many body system but is way too complex to just use it. The density functional theory (DFT) provides an innovative concept to reduce the computational costs considerably [45, 46]. Instead of searching for the ground state wavefunctions, the DFT searches for a ground state density $n(\mathbf{r})$. This reduces the number of degrees of freedom from $3N_{el}$ to 3.

We do not want to go into detail since there are a lot of excellent books which address the analytics behind density functional theory [17]. However, the Hohenberg-Kohn theorems as the basis of DFT, should not go unmentioned [45]:

Theorem 2.1. *The ground state energy can be described as a unique functional $E[n]$ of the electron density $n(\mathbf{r})$ which is given by the expectation value*

$$n(\mathbf{r}) = \langle \Psi | \sum_{i=1}^N \delta(\mathbf{r} - \mathbf{r}_i) | \Psi \rangle \quad . \quad (2.3)$$

Theorem 2.2. *The ground state density minimizes the ground state energy of the system, i.e. one has to deal with a variational problem:*

$$E_0 = E[n_0] \leq E[n] \quad (2.4)$$

$$\Rightarrow \frac{\delta E[n(\mathbf{r})]}{\delta n} = 0 \quad \text{with the side condition} \quad \int n(\mathbf{r}) d^3r = N \quad (2.5)$$

$$\Rightarrow \frac{\delta}{\delta n} \left\{ E[n(\mathbf{r})] - \mu \left(\int n(\mathbf{r}) d^3r - N \right) \right\} = 0 \quad . \quad (2.6)$$

Following these theorems, Kohn and Sham suggested a separation of $E[n]$ [46]:

$$E[n(\mathbf{r})] = T_s[n(\mathbf{r})] + \int v(\mathbf{r})n(\mathbf{r})d^3r + \frac{1}{2} \int \frac{n(\mathbf{r})n(\mathbf{r}')}{|\mathbf{r} - \mathbf{r}'|} d^3rd^3r' + E_{xc}[n(\mathbf{r})] \quad . \quad (2.7)$$

$T_s[n]$ represents the kinetic energy of non-interacting particles. Up to this point, everything is still exact. With the ansatz $n(\mathbf{r}) = \sum_{l=1}^N |\phi_l(\mathbf{r})|^2$ containing the non-interacting single-particle orbitals $\phi_l(\mathbf{r})$, an expression for $T_s[n]$ can be found. It also leads to the Kohn-Sham equations:

$$\left\{ \frac{\nabla^2}{2} + v(\mathbf{r}) + \frac{1}{2} \int \frac{n(\mathbf{r}')}{|\mathbf{r} - \mathbf{r}'|} d^3r' + \frac{\partial E_{xc}[n(\mathbf{r})]}{\partial n(\mathbf{r})} \right\} \phi_l(\mathbf{r}) = \epsilon_l \phi_l(\mathbf{r}) \quad (2.8)$$

All unknown many-body effects of $E[n]$ are put into $E_{xc}[n]$, the so-called exchange-correlation function. The real problem of DFT is that it is not possible to find an expression for E_{xc} (apart from an analytical solution for the homogenous electron gas) and approximations have to be made. The two most famous approximations are the local density approximation (LDA) ($E_{xc}^{LDA} = E_{xc}^{LDA}[n(\mathbf{r})]$) and the generalized gradient approximation (GGA) ($E_{xc}^{GGA} = E_{xc}^{GGA}[n(\mathbf{r}), \nabla n(\mathbf{r}), \nabla^2 n(\mathbf{r}), \dots]$). Both have to be determined numerically, e.g. with quantum Monte Carlo simulations, comparison with experimental data etc. There are a lot more possibilities to build a functional, e.g. hybrid functionals where an admixutre of Hartee-Fock exchange is included. But often accuracy comes with higher computational effort. One has to choose the functional fitting best to the problem. Common to all is that they are not able to describe all effects, especially quasiparticle effects [47, 48]. In this work we use norm-conserving PBE-functionals, spin-polarized GGA functionals suggested by Perdew, Burke and Ernzerhof [49]. The reason is simple: The systems, we want to investigate, consist of a high number of heavy atoms. This alone justifies the use of PBE-functionals as they provide a good balance between accuracy and computational effort, at least for the present problems. Additionally, spin-orbit coupling (SOC) becomes very important. In the following section, a new efficient approach is introduced, but the current implementation is only usable with norm-conserving pseudopotentials.

2.3 Relativistic quantum mechanics

As the title already mentions, this work deals with the influence of spin-orbit coupling on the electronic structure of different systems. For all calculations, we use the QUANTUM ESPRESSO package [16]. It already provides a spinor-based relativistic approach proposed by Andrea Dal Corso using full-relativistic pseudopotentials [50]. This method is very accurate but has two main problems: It is computationally demanding, which makes it difficult to use for big systems. And, the use of special pseudopotentials makes it less flexible and decreases the comparability with scalar-relativistic calculations. As part of this work, a new, fast method was developed that intends to avoid these problems.

As a starting point for the following derivation we choose the Dirac equation in the presence of external fields

$$(c\boldsymbol{\alpha} \cdot (\hat{\boldsymbol{p}} + \frac{1}{c}\mathbf{A}) + \beta mc^2 + V(\mathbf{r}) - E_{rel})\Psi = 0 \quad (2.9)$$

in the Foldy-Wouthuysen transformed gauge-invariant form [51, 52]

$$\begin{aligned} \hat{\mathcal{H}}_{FW} = \hat{g} \left[c^2 + \frac{(\hat{\boldsymbol{p}} + \frac{1}{c}\mathbf{A})^2}{2} - \frac{\hat{\boldsymbol{p}}^4}{8c^2} - \frac{1}{8c^2} \nabla \cdot \mathbf{E} + \varphi \right] \\ - \hat{\boldsymbol{\sigma}} \left[\frac{\mu_B}{2} \mathbf{B} + \frac{i}{8c^2} \nabla \times \mathbf{E} + \frac{1}{4c^2} \mathbf{E} \times (\hat{\boldsymbol{p}} + \frac{1}{c}\mathbf{A}) \right] . \end{aligned} \quad (2.10)$$

The first term of Equation (2.10) consists of the Darwin term and the kinetic energy correction which, in this form not well converging [53, 54], can be covered by using scalar-relativistic pseudopotentials. Without magnetic fields ($\mathbf{B} = 0$, $\mathbf{A} = 0$, $\nabla \times \mathbf{E} = -\frac{1}{c}\partial_t \mathbf{B} = 0$), the second part of $\hat{\mathcal{H}}_{FW}$ reduces to

$$\Delta \hat{\mathcal{H}}_{SO} = \frac{1}{4c^2} \hat{\boldsymbol{\sigma}} \cdot (\nabla V(\mathbf{r}) \times \hat{\boldsymbol{p}}) . \quad (2.11)$$

This term is known as the second-order approximation [55] and can be already found in Pauli theory. Together with scalar-relativistic pseudopotentials which include relativistic kinetic energy corrections, we get a proper relativistic description of electrons. Both, relativistic kinetic energy and spin-orbit coupling, are included. The use of the same pseudopotentials allows for a direct comparison of the scalar-relativistic and the SO-including calculations. So far, the method is only implemented for norm-conserving pseudopotentials exclusively. An extension to ultrasoft pseudopotentials is planned.

The so-called ‘‘Pauli-type’’ theory can now be further improved for heavy elements by using the zero-order regular approximation (ZORA) [56, 57]. With the Dirac Hamiltonian expanded in terms of $\frac{E}{2c^2 - V}$, we get

$$\tilde{\nabla}V = \nabla \left[\frac{2c^2}{1 - \frac{V}{2c^2}} \right] = \frac{1}{\left(1 - \frac{V}{2c^2}\right)^2} \cdot \nabla V \quad . \quad (2.12)$$

With $V \approx -\frac{Z}{r}$ the prefactor and thus the spin-orbit coupling is reduced with increasing atomic number.

For this (and further) work, the presented theory was implemented in the QUANTUM ESPRESSO package [16] by applying a two component version of Blöchl’s projector-augmented wave (PAW) transformation [58]

$$\hat{\mathcal{T}} = \hat{\mathcal{G}} + \sum_{\mathbf{R},m} [|\phi_{\mathbf{R},m}\rangle - \overline{|\phi_{\mathbf{R},m}\rangle}] \langle p_{\mathbf{R},m}| \quad (2.13)$$

on $\Delta\hat{\mathcal{H}}_{SO}$. Even though projectors $|p_{\mathbf{R},m}\rangle$ consist now of two components set up from scalar-relativistic components, they work just like in the original PAW transformation and are used to reconstruct the all-electron spinors $|\psi\rangle = \hat{\mathcal{T}} |\bar{\psi}\rangle$ from the pseudospinors $|\bar{\psi}\rangle$. The transformed all-electron Hamiltonian is given by

$$\begin{aligned} \overline{\Delta\hat{\mathcal{H}}}_{SO} &= \hat{\mathcal{T}}^\dagger \Delta\hat{\mathcal{H}}_{SO} \hat{\mathcal{T}} \\ &= \frac{1}{4c^2} \left[\hat{\boldsymbol{\sigma}} \cdot (\tilde{\nabla}V_{ps}(\mathbf{r}) \times \hat{\mathbf{p}}) + \underbrace{\sum_{\mathbf{R}} \sum_{n,m} |p_{\mathbf{R},n}\rangle f_{\mathbf{R},nm} \langle p_{\mathbf{R},m}|}_{=\hat{\mathcal{G}}_{\mathbf{R}}^{NL}} \right] \end{aligned} \quad (2.14)$$

with the matrix elements

$$f_{\mathbf{R},nm} = \langle \phi_{\mathbf{R},n} | \hat{\boldsymbol{\sigma}} \cdot \tilde{\nabla}V_{ae}(r) \times \hat{\mathbf{p}} | \phi_{\mathbf{R},m} \rangle - \langle \overline{\phi_{\mathbf{R},n}} | \hat{\boldsymbol{\sigma}} \cdot \tilde{\nabla}V_{ae}(r) \times \hat{\mathbf{p}} | \overline{\phi_{\mathbf{R},m}} \rangle \quad (2.15)$$

The nonlocal part $\sum_{\mathbf{R}} \hat{\mathcal{G}}_{\mathbf{R}}^{NL}$ reconstructs the all-electron contribution to the spin-orbit coupling.

By taking into account that (with more than 99 %) the major part of the spin-orbit coupling comes from the augmentation region, the first term of Equation (2.14) and the second term of Equation (2.15) are both small; in addition they nearly

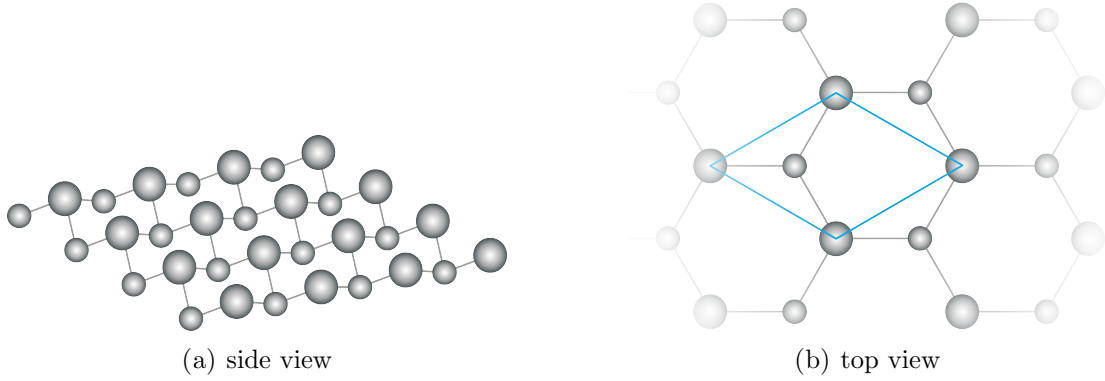


FIGURE 2.1: Schematic view of the Bi(111) bilayer. It is structurally similar to graphene but split into two sublattices separated by 1.67 Å. In blue the unit cell consisting of two Bi atoms is marked.

cancel each other. It remains

$$\overline{\Delta \hat{\mathcal{H}}_{SO}} = \frac{1}{4c^2} \sum_{\mathbf{R},n,m} |p_{\mathbf{R},n}\rangle \langle \phi_{\mathbf{R},n}| \frac{1}{r} \frac{\partial V_{ae}(r)}{\partial r} \times \hat{\boldsymbol{\sigma}} \cdot \hat{\mathcal{L}} |p_{\mathbf{R},m}\rangle \langle \phi_{\mathbf{R},m}| \quad , \quad (2.16)$$

the *reconstruction-only* form which decreases the computational costs significantly. Here $\hat{\mathcal{L}}$ stands for the angular momentum operator.

A perfect first test system to validate the presented method is the Bi(111) bilayer. As can be seen in Figure 2.1, it is structurally similar to graphene but the sublattices split up into two sublayers separated by 1.67 Å [60, 61]. Figure 2.2 compares the band structure of the bilayer calculated for different cases. Relativistic effects play indeed an important role here. Not only the kinetic energy correction but also the spin-orbit coupling lead to dramatic changes in the band structure. Below the Fermi energy E_F , three bands can be found with mainly p -character. At the Γ point, those bands cover a range of 0.5 eV in the scalar-relativistic case, whereby the second and third band are even degenerate. In the relativistic cases these two bands are separated by around 1.5 eV leading to an overall spreading of all three bands in a range of 2.3/2.5 eV (ZORA/full-relativistic) up to 3 eV (Pauli). In comparison with the full-relativistic reference band structure, the Pauli-type calculation reproduces the correct dispersion of the valence bands but underestimates the band gap and overestimates the overall splitting of the bands. With the ZORA both can be corrected and especially at the Fermi energy, the bands lie on top of each other.

Another quick test can be done for graphene. In the absence of spin-orbit coupling (SOC) it shows no energy gap but the typical Dirac points. Different theoretical

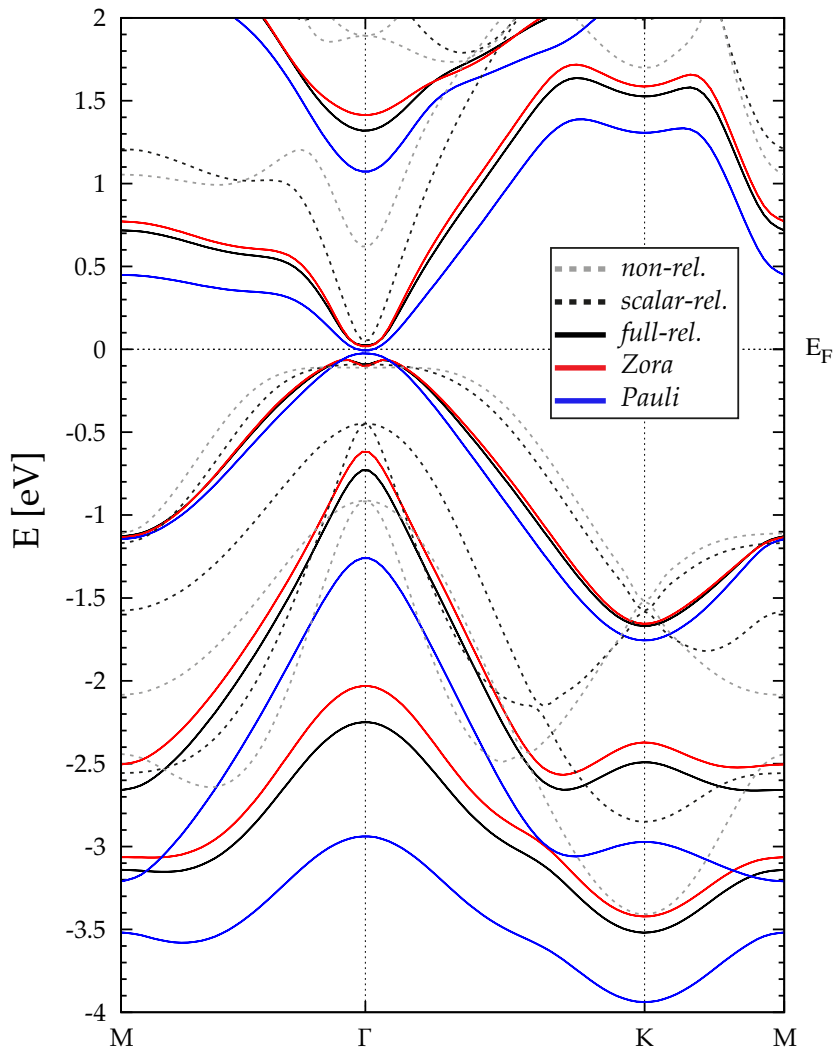


FIGURE 2.2: Band structure of a single Bi bilayer calculated in the non-relativistic case, the scalar-relativistic approximation, the full-relativistic approach by Dal Corso and the presented implementations of Pauli and ZORA-type spin-orbit Hamiltonians, where the relativistic band structure is reconstructed from scalar-relativistic pseudopotentials. Taken from own publication [59].

works have already predicted that SOC will lead to a gap opening at the K point and thus the existence of a low-temperature spin quantum Hall effect [62]. The energy gap ranges from relatively high 0.1 meV (tight-binding model) [62] over much lower 0.00086 meV (density functional theory (DFT) with full-relativistic LDA pseudopotentials) [63] to 0.05 meV (all-electron DFT) [64]. With our approach, using norm-conserving PBE pseudopotentials, we can get energy gaps over a big range depending on the used method and pseudopotential (see Table 2.1). There are nearly no differences of the values between the ZORA and Pauli approach. This proves that the ZORA only becomes really important when dealing with heavy atoms. In contrast to the Bi band structure where we could find no

deviation if using the full-potential (Equation (2.14)) or the *reconstruction-only* (Equation (2.16)) approach, we can see here obvious differences. When using a pseudopotential without including the d levels, we get a two orders of magnitude lower gap for the *reconstruction-only* approach as when using the full-potential version. If d electrons are included, we get (for all variations) a reasonable gap opening of 0.049 meV. This proves that the gap depends critically on the basis set. If the basis is too small, the gap opening becomes very small, too. The missing d electrons, or for another reason a too small basis, can explain the value of 0.00086 meV of [63].

For a more expanded review of the new method, systems showing a large Rashba effect and already investigated experimentally and theoretically, are used as further reference. The Bi-related surface alloys on noble metal substrates Bi/Cu(111) and Bi/Ag(111) are prototype examples for large Rashba effects at the Γ point of the Brillouin zone.

In a system where time-reversal symmetry holds, the transformation $t \rightarrow -t$ changes the momentum of an electron from \mathbf{k} to $-\mathbf{k}$ and inverts the spin. Thus, it holds $\epsilon(\mathbf{k}, \uparrow) = \epsilon(-\mathbf{k}, \downarrow)$. In a crystal with additional space inversion symmetry, it even holds $\epsilon(\mathbf{k}, \uparrow) = \epsilon(-\mathbf{k}, \uparrow)$. Time and space inversion symmetry combined lead to $\epsilon(\mathbf{k}, \uparrow) = \epsilon(\mathbf{k}, \downarrow)$ which means that the bands for spin-up and spin-down electrons are degenerate (also known as Kramer's degeneracy [67]). If the space inversion symmetry is broken, this degeneracy can be lifted due to SOC. The inversion asymmetry can be understood as an asymmetric potential perpendicular to the surface, $V(\mathbf{r}) \neq V(-\mathbf{r})$. Due to the now non-vanishing electric field, we get $\epsilon(\mathbf{k}, \uparrow) \neq \epsilon(\mathbf{k}, \downarrow)$, i.e. a momentum-dependent spin splitting is observed. Hence,

TABLE 2.1: Energy gap in meV for graphene calculated with different methods (ZORA/Pauli full-potential/reconstruction-only) and pseudopotentials (without or with d electrons). The gap becomes very small in the cases where the basis is too small.

	pseudopotential without d with d	
ZORA, Eq. (2.14)	0.03582	0.049
ZORA, Eq. (2.16)	0.00076	0.049
Pauli, Eq. (2.14)	0.03582	0.049
Pauli, Eq. (2.16)	0.00074	0.049
collinear (001), Eq. (2.14)	1.943900	
collinear (001), Eq. (2.16)	2.142280	

TABLE 2.2: Rashba parameters of Bi-related surface alloys, calculated at the Γ point with different approaches (Dal Corso and ZORA/Pauli within the full-potential or *reconstruction-only* version) and compared with experimental results and former all-electron DFT calculations. Taken from own publication [59].

System [Ref.]	E_R [meV]	Δk [\AA^{-1}]	α_R [eV\AA]
Bi/Cu(111) surf. alloy Exp. [65]	13	0.032	0.82
DFT [65]	9	0.028	0.62
full-relativistic (Dal Corso)	14.5	0.032	0.89
ZORA, Eq. (2.14)	12.7	0.027	0.94
ZORA, Eq. (2.16)	12.7	0.027	0.94
Pauli, Eq. (2.14)	13.3	0.028	0.95
Pauli, Eq. (2.16)	13.3	0.028	0.95
Bi/Ag(111) surf. alloy Exp. [66]	200	0.13	3.05
DFT [66]	145	0.10	2.90
full-relativistic (Dal Corso)	144	0.082	3.63
ZORA, Eq. (2.14)	145	0.085	3.38
ZORA, Eq. (2.16)	145	0.085	3.38
Pauli, Eq. (2.14)	168	0.100	3.37
Pauli, Eq. (2.16)	168	0.100	3.37

the Rashba effect is a direct consequence of the spin-orbit coupling². It was discovered in 1959 by Emmanuel Rashba [69, 70]. The corresponding Hamiltonian can be derived directly from the SOC-Hamiltonian (Equation (2.11)) by assuming an effective potential gradient along z and introducing the so-called Rashba parameter α_R :

$$\hat{\mathcal{H}}_R = \alpha_R \hat{\boldsymbol{\sigma}} \cdot (\mathbf{e}_z \times \mathbf{k}) \quad (2.17)$$

$$= \alpha_R (\hat{\sigma}_x k_y - \hat{\sigma}_y k_x) \quad (2.18)$$

$$= \begin{pmatrix} 0 & \alpha_R(k_y + ik_x) \\ \alpha_R(k_y - ik_x) & 0 \end{pmatrix} \hat{g} \quad (2.19)$$

with the eigenvalues $\varepsilon_{\pm}^R = \pm \alpha_R k$. If we start from an ideally parabola shaped band with its extremum at (E, k) , the Rashba effect leads to a splitting of this band into

²Related to the Rashba effect is the so-called Dresselhaus effect [68] which appears for zinc blende structures, e.g. III-V semiconductors. The corresponding Hamiltonian is $\hat{\mathcal{H}}_D = \alpha_D (\sigma_y k_y - \sigma_x k_x)$

two parabolas with the energies:

$$\begin{aligned}
 E_{\pm} &= \frac{k^2}{2m^*} \pm \alpha_R k \\
 &= \frac{1}{2m^*} \left(k \pm \underbrace{\alpha_R m^*}_{\Delta k} \right)^2 - \underbrace{\frac{\alpha_R^2 m^*}{2}}_{E_R}
 \end{aligned}
 \tag{2.20}$$

The Rashba parameter α_R can thus be defined as

$$\alpha_R = \frac{2E_R}{\Delta k} = \frac{\Delta k}{m^*}
 \tag{2.21}$$

Table 2.2 compares all methods (Dal Corso and ZORA/Pauli within the full-potential or *reconstruction-only* version) as well as former all-electron DFT calculations and the experiment regarding the characteristic quantities with E_R and Δk being the energy and k -point shift and α_R as the Rashba parameter for the two systems Bi/Cu(111) and Bi/Ag(111). In the same way as before, the *reconstruction-only* and the full-potential calculations lead to exactly the same values. Those are in good agreement with the experiment and even slightly better than the all-electron DFT calculations. The formerly implemented relativistic method by A. Dal Corso, too, provides satisfactory results, but at a much higher computational costs. By using the new approach the computational time can be reduced by 30 % or even 60 % when using the *reconstruction-only* version. For comparison, the scalar-relativistic calculation of such a systems only takes 8 % of the time the full-relativistic calculation needs.

Chapter 3

In/Si(111) nanowires

Quasi one-dimensional systems are of great scientific and technological interest. Due to their low dimensionality these systems have special properties, e.g. quantization of conductance, phase transitions and many more. Metallic nanowires are prototype 1D systems. One of those prototypes is given by indium-nanowires that self-organize on the silicon (111) surface. The In surface states are located almost completely inside the Si band gap which makes it a great model for 1D systems. Despite being one of the most investigated atomic wire systems, experimentally and theoretically, there are still lots of properties left to study. The aim to build smaller and smaller electronic components will profit from the understanding of the mechanisms and properties of this atomic sized system.

Indium was first discovered and described by the German chemists Ferdinand Reich and Theodor Richter in 1863 [71, 72]. It is a soft silver-white post-transition metal and can be used for a wide range of applications. InN, for example, is a group-III-nitride and just as the famous GaN is suitable for semiconductors and related devices [73]. In everyday life, indium is used in alloys with Cd, Zn, Bi, etc. Those have low melting points of 50 – 100 °C and thus can be used in thermostats or fire sprinkler systems [74].

J.J. Lander and J. Morisson were the first who applied indium on the silicon (111) surface [75]. With low-energy electron diffraction (LEED) analysis, they found the famous (4×1) reconstruction but they were not aware of the quasi-1D character of the system they had in front of them. Angle-resolved photoemission spectroscopy (ARPES) [76, 77] and scanning tunneling microscopy (STM) [77] measurements 30 years later confirmed the existence of metallic In-nanowires.

3.1 Crystal structure and modelling

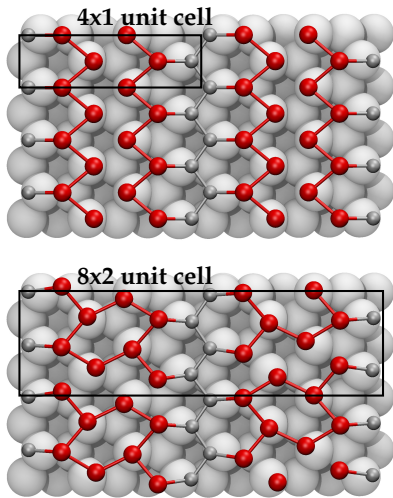


FIGURE 3.1: Schematic view of the (4×1) structural model for the RT phase of In/Si(111) (top) and the (8×2) hexagon model for the LT phase (bottom). Taken from own publication [59].

One of the most prominent features of the In-nanowires on Si(111) is a temperature-driven metal-insulator phase transition. At room temperature (RT) ordered arrays of In-nanowires are formed with a (4×1) surface periodicity, but at low temperatures ($T = 120$ K) a rearrangement of the In double chain takes place and, thus, hexagons are formed as can be seen in Figure 3.1 leading to a (8×2) periodicity. This phase transition is reversible and has a significant impact on the electronic properties. Whereas the RT phase is metallic, the low temperature (LT) phase becomes semiconducting with a band gap of about 0.1 eV (cf. Figure 3.2).

Even though the (4×1) reconstruction was already discovered in 1965 [75], the corresponding structural model was not determined until 34 years later by Bunk et al. [78]. Each nanowire consists of two zigzag chains of In with a (4×1) surface periodicity. The nanowires are separated by Si chains resembling the chains of the clean Si(111)- (2×1) surface (cf. Figure 3.1 top). Shortly after the (4×1) model was established, the semiconducting (8×2) was experimentally discovered [79]. Often seen in scanning tunneling microscopy (STM) [79–83], the atomic structure of this phase was unclear until González et al. proposed a hexagonal structural model which is in agreement with various experimental data [84, 85]. Here, the In double chain experiences a displacement of ± 0.35 Å along the direction of the chain leading to a hexagonal arrangement of the In atoms (cf. Figure 3.1 bottom)

For the simulation of the In/Si(111)- (4×1) as well as the (8×2) surface three Si bilayers are used. The bottom layer is terminated with hydrogen. The hydrogen layer and the bottom Si bilayer are kept fixed. Hence, we have just 34 atoms in the (4×1) cell and 136 atoms in the (8×2) cell. As \mathbf{k} -point sampling $16\times 4\times 1$ respectively $8\times 2\times 1$ were used. For both phases, a cutoff energy of 50 Ry is found to be sufficient.

With an atomic number of 49 Indium is a relatively heavy atom. Hence, it is no wonder that In-containing systems often show comparatively large relativistic effects [86, 87]. After an antiferromagnetic spin ordering was found in gold chains on silicon surfaces [88], it is worth investigating relativistic effects for the In-nanowires. For that, the relativistic approach presented in Section 2.3 is suitable. In its *reconstruction-only* form, both the (4×1) phase with just 34 atoms and the (8×2) phase with 136 atoms can be treated without needing too much computational time.

Stekolnikov et al. have shown that the energetic and structural properties of the In/Si(111) surface depends critically on the treatment of the d -electrons, whether they are treated as core or valence electrons, as well as on the use of the functional, local density approximation (LDA) or generalized gradient approximation (GGA) [89]. Furthermore, Kim and Cho have shown that it makes a difference whether van der Waals (vdW) interaction is taken into account or not [90]. All in all, the system and the phase transition depends very much on the lattice constant of the substrate and the In-In bond length on top.

The calculations presented in this work are all valid at absolute zero temperature. Thus, the (8×2) -LT phase should be energetically favored. This can only be achieved within the local density approximation. With GGA, we either get a less stable minimum (using PW91) or no stable minimum at all (using PBE) [59]. LDA, even in combination with scalar-relativistic pseudopotentials and the new relativistic ZORA approach, (Sec. 2.3) leads to a hexagon model that is at least ≈ 7 meV per In atom more stable than the zigzag chain model.

3.2 Rashba splitting

Most of the results in this chapter can be found in the related publication:

U. Gerstmann, N. J. Vollmers, A. Lücke, M. Babilon, and W. G. Schmidt
Rashba splitting and relativistic energy shifts in In/Si(111) nanowires
 Physical Review **B** 89, 165431 (2014)

By including spin-orbit coupling in the calculation, we have already seen for the bismuth bilayer (cf. Figure 2.2 in Section 2.3) that the band structure reveals some new interesting features. The band structure of the In-nanowires at Si(111) is

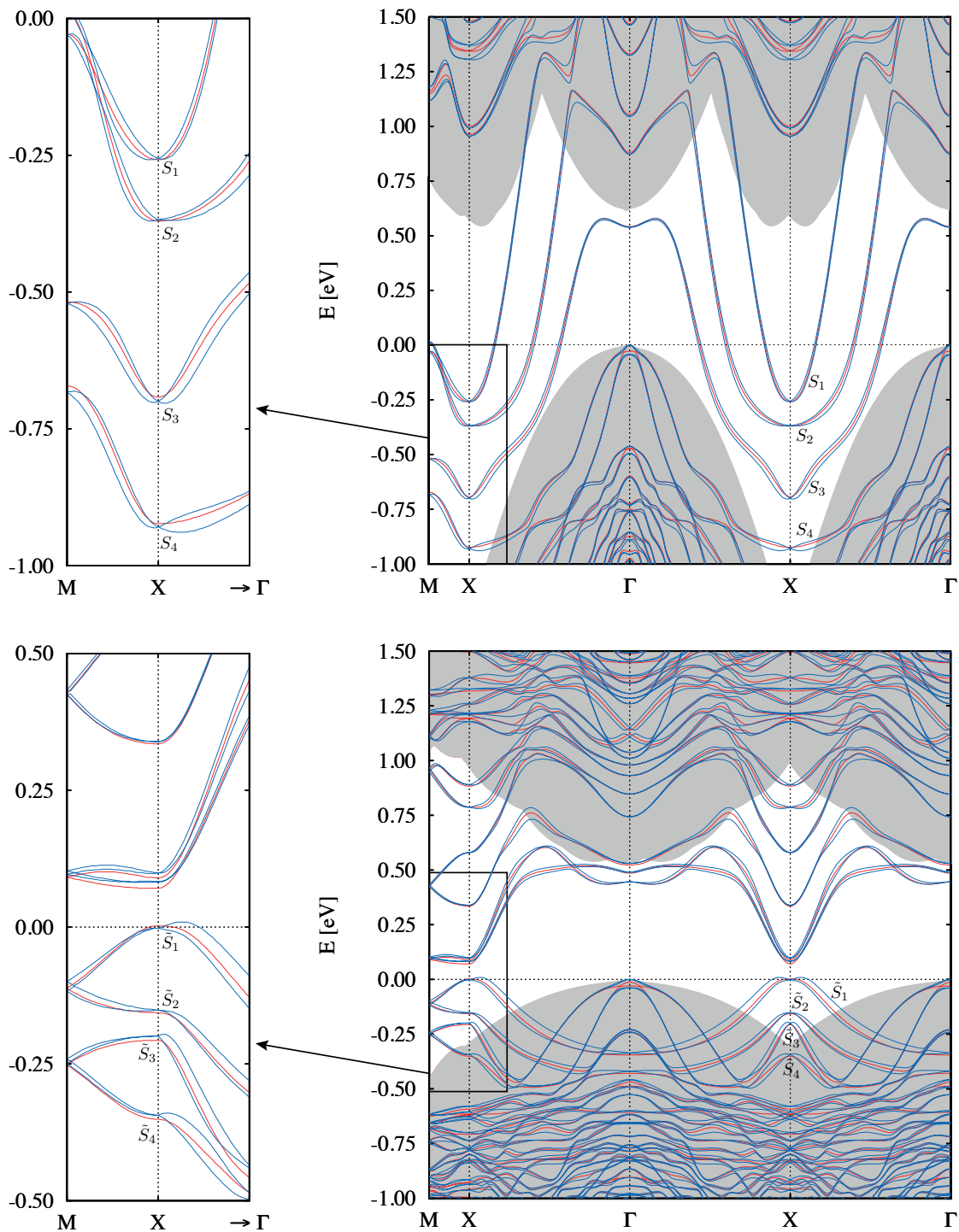


FIGURE 3.2: Scalar-relativistic (red) and full-relativistic (blue) band structures calculated for the In/Si(111) (4×1) (top) and (8×2) (bottom) phase. k_x is the direction parallel and k_y the direction perpendicular to the In chains. In grey, the silicon bulk band structure is visible which also defines the zero with its valence band maximum. At the X point strong anisotropic Rashba splittings can be found. Taken from own publication [59].

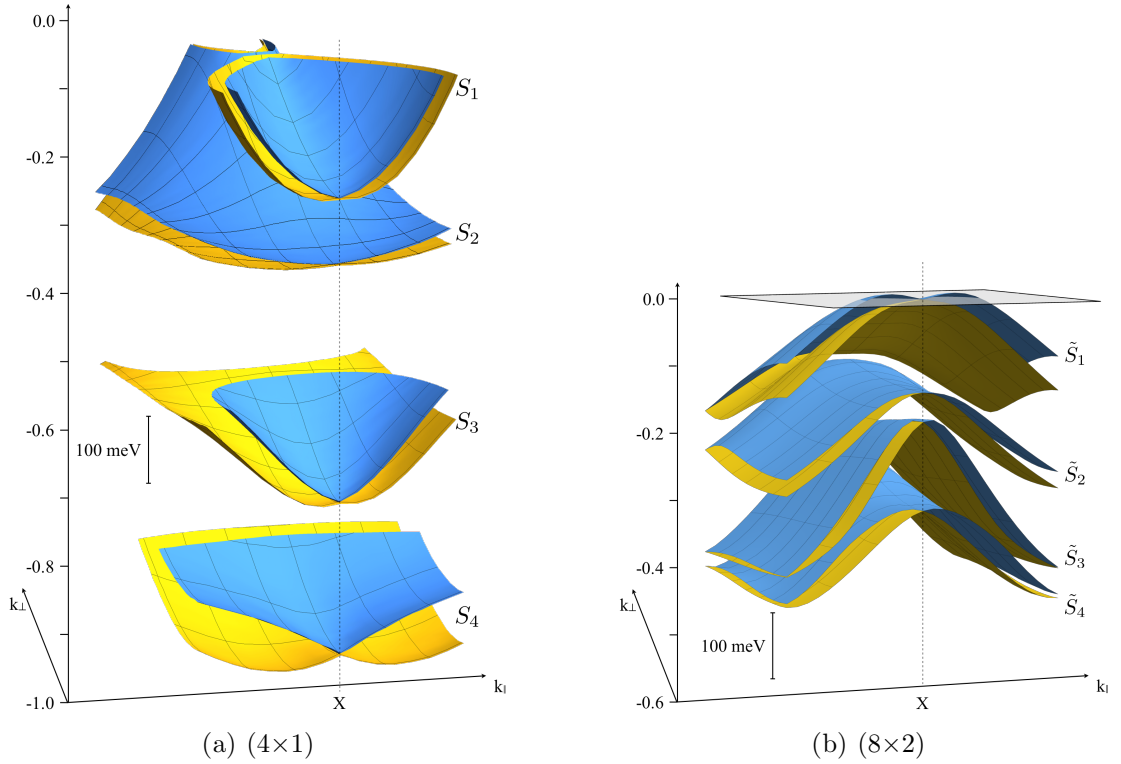


FIGURE 3.3: Calculated energy dispersion $E(k_{\parallel}, k_{\perp})$ of the In-related surface state around the X point showing in more detail the Rashba effect that is revealed by including spin-orbit coupling in the calculation. The two spin channels are indicated by different colors. Taken from own publication [59].

displayed in Figure 3.2. A comparison of the red scalar-relativistic band structure with the blue full-relativistic one (here: ZORA within the *reconstruction-only* version) shows that the band structure does not change its form, but the spin degeneration of the bands is lifted. First, we bring our attention to the Γ point. The largest energy splittings for the occupied bands can be found here. With a value of 43 meV for the (4×1) and 39 meV for the (8×2) phase, the valence band splitting of silicon bulk can be reproduced [96]. For the conduction bands we have to look at the X point. The splitting amounts to 65 meV for the (4×1) and 28 meV for the (8×2) phase at around 1.3/1.2 eV above the valence band maximum.

More interestingly a Rashba effect becomes visible at the X point for both phases. Here, mainly the four In-related surface bands S_1 , S_2 , S_3 and S_4 (\tilde{S}_1 , \tilde{S}_2 , \tilde{S}_3 and \tilde{S}_4) show strong shifts in k as well as strong energy splittings for both, the room temperature (RT) phase and the low temperature (LT) phase. The Rashba effect is well understandable as the inversion symmetry of the In-wires is broken by the Si substrate which alone occurs for big changes in the band structure. Further structural modifications, especially due to a charge-density wave formation in the

(8×2) phase [79], underpin this. The left part of Figure 3.2 shows the Rashba-split bands in more detail. The anisotropy of the Rashba effect becomes apparent, especially for the bands S_4 of the (4×1) and all In-related bands of the (8×2) phase. It is even more obvious when regarding a three-dimensional version of the band structure around the X points as illustrated in Figure 3.3.

Table 3.1 compares the so-called Rashba parameters of the In/Si(111) nanowires with different well investigated systems. The energy splitting E_R is with up to 11 meV for the LT phase in the range of that of the Bi(111) surface and even one magnitude larger than that of other indium containing systems like InGaAs/InAlAs but with a similar splitting in \mathbf{k} -space, $\Delta k \approx 0.021 \text{ \AA}^{-1}$. The resulting Rashba parameter $\alpha_R = 1.047 \text{ meV \AA}$ lies inbetween the ones of Bi/Cu(111)

TABLE 3.1: Calculated spin-orbit splitting at the X point for the In-related surface bands of In/Si(111) nanowires are compared with literature data and calculations for other surfaces (Γ point). The Rashba energy of the split states E_R , the wave number offset Δk (from the reference point) and the Rashba parameter $\alpha_R = 2E_R/\Delta k = \frac{\hbar\Delta k}{m^*}$ are given. Taken from own publication [59].

system [Ref.]	E_R [meV]	Δk [\AA^{-1}]	α_R [meV \AA]
InGaAs/InAlAs [86, 87]	<1	0.028	0.07
Cu(111) surface [91]	≈ 0	≈ 0	≈ 0
Ag(111) surface [92]	<0.2	0.004	0.03
Au(111) surface [93, 94]	2.1	0.012	0.33
Bi(111) surface [95]	14	0.05	0.56
<hr/>			
In/Si(111) (4×1): $S_1(\parallel k_x)$	1.2	0.009	0.267
$S_1(\parallel k_y)$	3.0	0.020	0.300
(4×1): $S_2(\parallel k_x)$	1.6	0.022	0.145
$S_2(\parallel k_y)$	2.8	0.020	0.280
(S_1, S_2 average)			(0.248)
(4×1): $S_3(\parallel k_x)$	3.4	0.013	0.523
$S_3(\parallel k_y)$	2.0	0.010	0.400
(4×1): $S_4(\parallel k_x)$	9.0	0.044	0.409
$S_4(\parallel k_y)$	1.3	0.007	0.371
(S_3, S_4 average)			(0.426)
<hr/>			
In/Si(111) (8×2): $\tilde{S}_1(\parallel k_x)$	11.0	0.021	1.047
$\tilde{S}_1(\parallel k_y)$	<0.05	<0.005	—
(8×2): $\tilde{S}_2(\parallel k_x)$	<0.1	<0.001	—
$\tilde{S}_2(\parallel k_y)$	<1.5	0.017	0.176
(8×2): $\tilde{S}_3(\parallel k_x)$	3.6	0.007	1.028
$\tilde{S}_3(\parallel k_y)$	<0.05	<0.005	—
(8×2): $\tilde{S}_4(\parallel k_x)$	3.4	0.011	0.618
$\tilde{S}_4(\parallel k_y)$	<0.05	<0.005	—

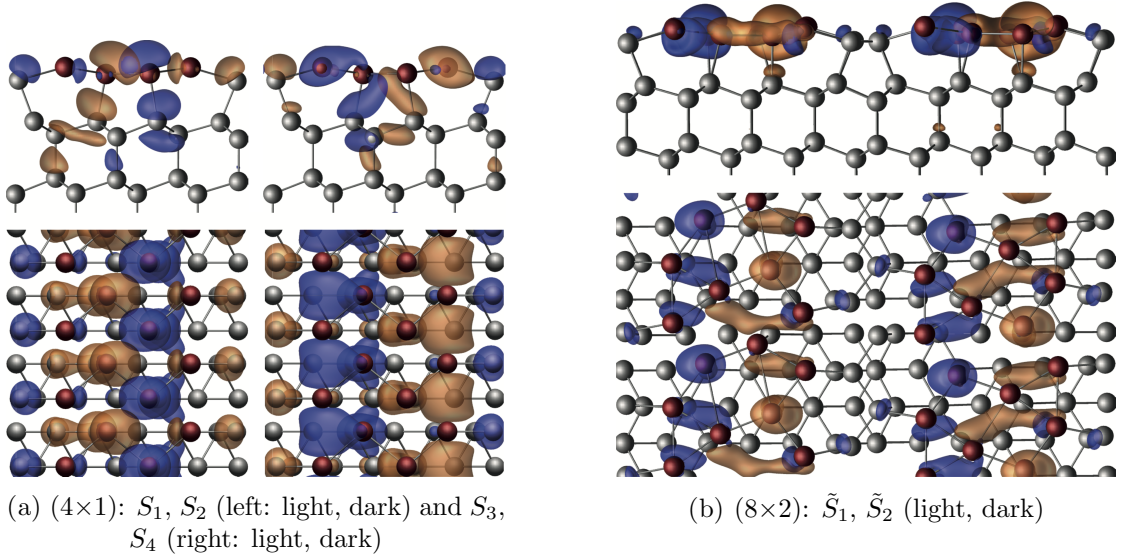


FIGURE 3.4: Visualization of the orbital character of the In-related bands at the X point. In the case of the RT phases, a high p_x contribution of the bands located mainly at the outer In atoms leads to the large Rashba splitting along the wire direction. Taken from own publication [59].

and Bi/Ag(111) (cf. Tab. 2.2 in Sec. 2.3), which are known to be textbook examples for Rashba splitting. Here, the Bi atoms enhance the already present, but nearly invisible Rashba effect of the noble metal surface. The same is true for the In-nanowires which enhance the Rashba effect undetectable for the pure Si(111) surface.

To understand the origin of the Rashba effect in this system, we have to go back to theory. In Section 2.3, we have seen that the spin-orbit Hamiltonian in the

TABLE 3.2: Decomposition of the In 5p surface bands into the prozentual p_x, p_y, p_z contributions for the (8×2) hexagon structure and the (4×1) zigzag chains of the In-nanowire. Taken from own publication [59].

phase	band	$(E_R)_x$ [meV]	$(E_R)_y$ [meV]	p_x [%]	p_y [%]	p_z [%]
(4×1)	S_1	1.2	3.0	9.2	32.2	58.6
	S_2	1.6	2.8	4.9	22.1	73.0
	S_3	3.4	2.0	59.7	26.5	13.7
	S_4	9.0	1.3	54.8	19.3	25.8
(8×2)	\tilde{S}_1	11.0	0.1	68.9	16.8	14.3
	\tilde{S}_2	0.1	1.5	77.2	3.8	18.9
	\tilde{S}_3	3.6	0.1	80.6	6.9	12.5
	\tilde{S}_4	3.4	0.1	86.3	5.2	8.6

absence of magnetic fields is, cf. Eq. (2.11):

$$\Delta\hat{\mathcal{H}}_{SO} = \frac{1}{4c^2}\hat{\boldsymbol{\sigma}} \cdot (\nabla V(\mathbf{r}) \times \hat{\mathbf{p}}) \quad (3.1)$$

We can now substitute $\mathbf{p} = \mathbf{k}$ and assume an effective potential gradient along z , i.e. $\nabla V = \partial_z V \mathbf{e}_z$. With effective masses m_x^* and m_y^* in the Rashba parameter $(\alpha_R)_i = \frac{\Delta k}{m_i^*}$ we get the spin-orbit Hamiltonian in \mathbf{k} -space (see also Equation (2.19)):

$$\Delta\hat{\mathcal{H}}_{SO}(\mathbf{k}) = (\alpha_R)_y \cdot \hat{\boldsymbol{\sigma}}_x k_y - (\alpha_R)_x \cdot \hat{\boldsymbol{\sigma}}_y k_x \quad (3.2)$$

It holds $\mathbf{k} = \mathbf{p} = \frac{\nabla}{i}$. Therefore the orientation of the p orbitals in real space determines the orientation of the k_x and k_y related contribution to the Rashba effect. In Table 3.2 the different contributions of p_x , p_y and p_z to the In related bands are listed for the (4×1) and the (8×2) phase. For the (4×1) phase, the Rashba splittings can be well explained. Figure 3.4 shows the orbital character of the upper surface bands S_1 (orange) and S_2 (blue). Both bands are localized at the inner In atoms. They correspond mainly to orbitals with p_z character, 58.6% and 73.0% (cf. Table 3.2). These are oriented along the surface normal and do not couple with available spin degrees of freedom. Hence, they do not contribute to any in-plane splitting. The p_y contribution is roughly three times larger than the p_x contribution and located at the outer In atoms. This results in a larger splitting in k_y direction, perpendicular to the nanowires. From this alone, we can conclude that mainly the outer In atoms are responsible for the Rashba effect. With our code (within the *reconstruction-only* version) it is possible to turn on the spin-orbit coupling just for specific atoms and so we can easily confirm the last conclusion. The band structure of the RT phase (Figure 3.2 (top)) changes only slightly and the Rashba splitting is still present which means the same finding can be transferred to the other two bands S_3 and S_4 . Here, the correspondence between the p orbitals and the Rashba splitting becomes even more obvious, cf. Table 3.2 and Figure 3.4 (a) right. More than 50% p_x contribution lead to a large Rashba splitting in k_x . The p_x orbitals provide a conductivity channel along the wire direction and are therefore responsible for the conducting character of the (4×1) phase.

Whereas the explanation of the anisotropic Rashba splitting is relatively straightforward for the (4×1) phase, it becomes more complicated for the (8×2) phase. The four In-related surface bands \tilde{S}_1 , \tilde{S}_2 , \tilde{S}_3 and \tilde{S}_4 have a similar contribution of the p_x orbitals as S_3 and S_4 of the RT phase. One would expect, thus, similar

Rashba splittings. With a vanishing splitting perpendicular to the In-nanowires, the anisotropy is even bigger for the LT phase. But there is one exception. The \tilde{S}_2 band's splitting is inverted and in k_x direction it is actually nearly zero even though the contribution of the p_x orbital amounts to 77.2%. The population of the p orbitals does not provide any explanation. Again we restrict the spin-orbit coupling to the inner and outer atoms and get the same band dispersion but something new pops up. The two In subsets show reversed spin polarization for the k_x direction of \tilde{S}_2 and the k_y direction of the other bands. This means a superposition of all bands results in a cancellation of the spin-dependent splitting. Thereby, in particular the \tilde{S}_1 band shows an interesting feature. Its position to the Fermi level defines the top of the valence bands which is 30 meV above the valence band maximum of the silicon bulk. Therefore the resulting Rashba effect is not protected by the substrate. The Rashba-split \tilde{S}_1 bands should easily be depopulated which may be used for spin filtering by external fields. Experimental work into this direction is already in preparation.

Chapter 4

The bismuth (111) surface

Bismuth (Bi) is one of the first ten metals to have ever been discovered. As early as in the 16th century, the outstanding physical properties of this material were known. Often confused with other elements like lead and tin, bismuth was described as an own element in 1753 by French chemist Claude-François Geoffroy [97]. It is a silver-white crystalline metal but due to oxidation it often appears in rainbow-like colors (Figure 4.1). Bismuth is a relatively rare element which can be found in its pure form in Australia, Bolivia and China. The commonest naturally compounds of bismuth are bismuthinite (Bi_2S_3) and bismite (Bi_2O_3). Pure bismuth can be obtained by reduction [74], e.g. $2 \text{Bi}_2\text{O}_3 + 3 \text{C} \longrightarrow 3 \text{CO}_2 + 4 \text{Bi}$.

Since bismuth is a brittle metal, it is often used in alloys with other metals like tin or cadmium. For example, Wood's metal (50% Bi, 25% Pb, 12.5% Cd and 12.5% Sn) has a low melting point of around 60°C and is therefore used for fire sprinkler systems and electric fuses [74].

Bismuth-209 was long regarded as the heaviest stable isotope but there have been theoretical predictions against this assumption [98]. These predictions were experimentally verified in 2003, when French researchers measured an α -decay half-life



FIGURE 4.1: Bismuth crystal. Normally a silver-white metal, it often appears colorful due to oxidation. (own photograph)

of Bi of $1.9 \cdot 10^{19}$ yr [99]. This makes bismuth one of the few elements where radioactivity was theroretically predicted before being experimentally detected.

In the last years, a new class of materials gained a lot of attention, topological insulators. A topological insulator has a bulk energy gap but also has conducting surface states that are protected by time-reversal symmetry. Most realized topological insulators exhibit a strong spin-orbit coupling (SOC) and are therefore candidates for future applications in spintronics. Prototypes for topological insulators are Bi_2Se_3 , Bi_2Te_3 and other Bi-containing materials. Bismuth itself cannot be classified as a topological insulator as it has no protected surface states. However, it has spin-split surface states and can serve as a model system for some of the properties of topological insulators [100]. Recently bismuth bilayers are found to have even topological edge states themselves [60, 101]. A lot of former research addresses the manipulation of electron transport in the surface states by the deposition of adatoms [102, 103]. The adatoms at the surface influence the bismuth layers underneath. In this work, a new type of surface manipulation is presented where $3d$ transition metals (TMs) are built *barrier-free* into a well-defined position within the uppermost bismuth bilayer of the bismuth (111) surface and without changing the surface topography.

4.1 The Bi(111) surface

4.1.1 Technical details

The electron configuration of Bismuth is $[\text{Xe}]4f^{14}5d^{10}6s^26p^3$. It is known that in solids the s and p levels will mix but the closed-shell d -electron levels and the core-electron levels do not change. Therefore we treat the $6d$ electrons as core electrons in our pseudopotential and take only the $6p$ and $6s$ as valence electrons into consideration, i.e. in total five valence electrons. This was carefully tested. With PBE the, in this way, determined pseudopotential gives the best agreement with the experimental structure of bismuth bulk and the bismuth (111) surface. We use $3d$ transition metals (TMs) as adatoms wherby we choose cobalt as example TM. The electron configuration of Cobalt is $[\text{Ar}]3d^74s^2$. As a “late” $3d$ TM, the so-called $3s$ and $3p$ “semi-core electrons” can be reasonably described within the core. The electrons of the partially filled $3d$ shell explicitly take part

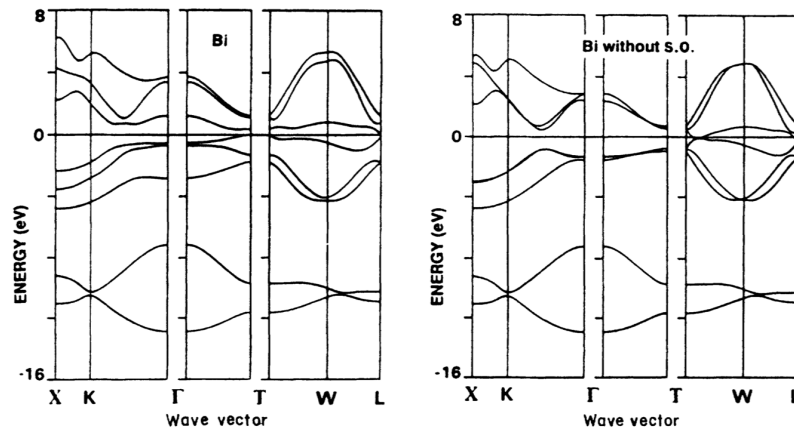


FIGURE 4.2: One of the first *ab initio* DFT band structure calculations of bismuth bulk done by Gonze et al. [104]. SOC is included by using full-relativistic pseudopotentials. The only experimental values used in their work are the crystallographic parameters. At close inspection at the L point, a small overlap at the Fermi energy between conduction and valence bands becomes visible. Another overlap is found at the T point but vanishes when SOC is included.

in the bonding behaviour. Hence, our norm-conserving pseudopotential contains 9 valence electrons, the $3d$ and $4s$ electrons.

$3d$ TMs usually are magnetic. To get a converged magnetic moment, we have to use at least a $24 \times 24 \times 1$ Monkhorst-Pack \mathbf{k} -point grid for a (1×1) Bi(111) unit cell. Besides this large number of \mathbf{k} -points, the TM atoms have the disadvantage that they need a very high energy cut-off of $90 \text{ Ry} \approx 1225 \text{ eV}$.

For this work, an additional property of bismuth is important, the strong spin-orbit effects. Because of its high mass, relativistic effects cannot be neglected. For a structural analysis, a scalar-relativistic description is sufficient. But for all electronic properties, e.g. already the band structure, we have to use the relativistic approach presented in Section 2.3.

4.1.2 Crystal structure

Bismuth is a group V semimetal. This means at most points of the Brillouin zone exists an energy gap like in a semiconductor but there are points, here the L point, where a small overlap between valence and conduction bands can be found, see Figure 4.2, making bismuth formally a metal. The comparison of the band structure with and without spin-orbit coupling (SOC) reveals the importance of including SOC in the calculation. In the calculation for Figure 4.2 this was done by using full-relativistic pseudopotentials [104]. The shape of the band structure

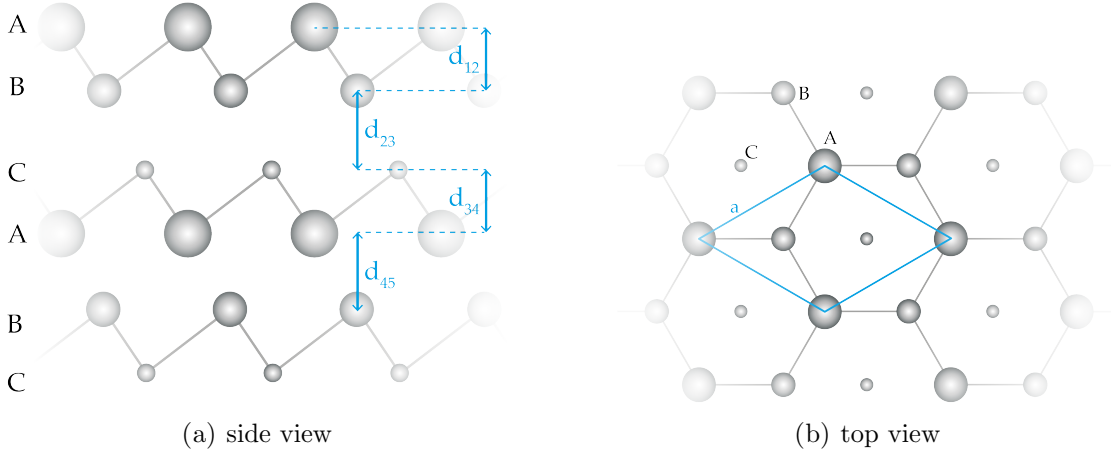


FIGURE 4.4: Schematic view of the clean Bi(111) surface. In blue the notation for the bulk interlayer distances (left) and the unit cell are marked (right). In the ideal bulk it holds $d_{12} = d_{34}$ etc. and $d_{23} = d_{34}$ etc.

is roughly the same, but the degeneracy of the bands around the Fermi energy is lifted. Additionally, a gap opens at the T point and gives rise to a hole pocket.

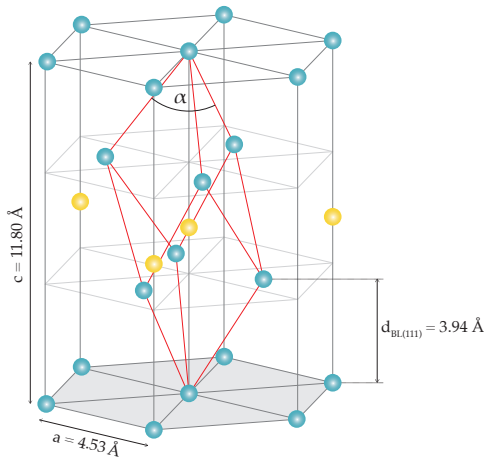


FIGURE 4.3: Bismuth bulk structure with the rhombohedral unit cell (red) and the hexagonal cell. The two atoms of the rhombohedral cell are marked in blue and yellow. (after [105, 106])

with its puckered bilayers is very convenient for us since we want to investigate the Bi(111) surface.

The bismuth (111) surface consists of different layers which are arranged as bilayers. The surface has a three- or sixfold symmetry with respect to the numbers of bilayers. Figure 4.4 shows a schematic top and side view of the Bi(111) surface. As a reference for comparing structural changes we use the so-called truncated bulk

Like all group V elements bismuth crystallizes in a rhombohedral cell with a two-atomic base illustrated in red in Figure 4.3. The lattice parameter is $a_{rh} = 4.72 \text{ \AA}$ and the angle between the lattice vectors is $\alpha = 57.35^\circ$ instead of the “ideal” 60° [107]. Each atom has three nearest neighbors and three next-nearest neighbors. This results in covalently joined bilayers along the (111) direction (cf. also Figure 2.1 in Section 2.3). It is possible to translate the rhombohedral lattice into a hexagonal one pointing in (111) direction. The lattice parameters are then $a_{hex} = 4.53 \text{ \AA}$ and $c = 11.80 \text{ \AA}$ [107, 108].

structure, i.e. the crystal is terminated with a Bi bilayer. In blue the unit cell is marked. A lattice constant of $a = 4.53 \text{ \AA}$ was experimentally derived from low-energy electron diffraction (LEED) measurements [108]. This results in a distance between two bilayers (long interlayer distance) in the truncated bulk structure of $d_{23} = d_{45} = \dots = 2.35 \text{ \AA}$ and a short interlayer distance of $d_{12} = d_{34} = \dots = 1.59 \text{ \AA}$. In our PBE calculations the lattice constant is slightly overestimated by 2% with $a = 4.63 \text{ \AA}$. Therefore the interlayer distances are slightly different from the experimental values with $d_{12} = 1.57 \text{ \AA}$ and $d_{23} = 2.47 \text{ \AA}$. In the following, when referred to the (truncated) bulk, the PBE calculated one is meant for better comparison with the following calculations. It should be noted that the influence of slight structural modifications (like the PBE deviation) was tested and no relevant changes were seen in the band structure or Fermi surface. The influence of the modification of bilayer distances was also examined by Du et al. in their recent publication [109] (cf. Figure 4) based on relativistic all-electron calculations.

4.1.3 Modeling of the surface

The first question that arises when modeling the Bi(111) surface is how many Bi bilayers have to be taken into account. Yu. M. Koroteev et al. have already addressed this matter [61]. Figure 4.5 shows the change in the band structure of the clean Bi(111) surface when increasing the number of bilayers. In a nice addition, the large influence of SOC is illustrated for one and two bilayers. With SOC the band structure looks very different and can change from metallic to semimetallic where the valence and conduction band just touch the Fermi level but do not cross it. Only for Bi(111) films with more than four bilayers the surface shows truly metallic behavior and surface states that cross the Fermi level resulting in electron and hole pockets. The authors stated that from ten bilayers on only minor changes of the band structure can be expected. Figure 4.5 proves that even a slab with six bilayers provides a nearly converged band structure and thus can be set as a minimum number of bilayers one should take into account. As we will see in Section 4.2 for a structural description of what happens if adatoms come into play, three bilayers with the bottom bilayer kept fixed are sufficient. Here, the distance from the fixed to the first free bilayer coincides automatically with the corresponding bulk value.

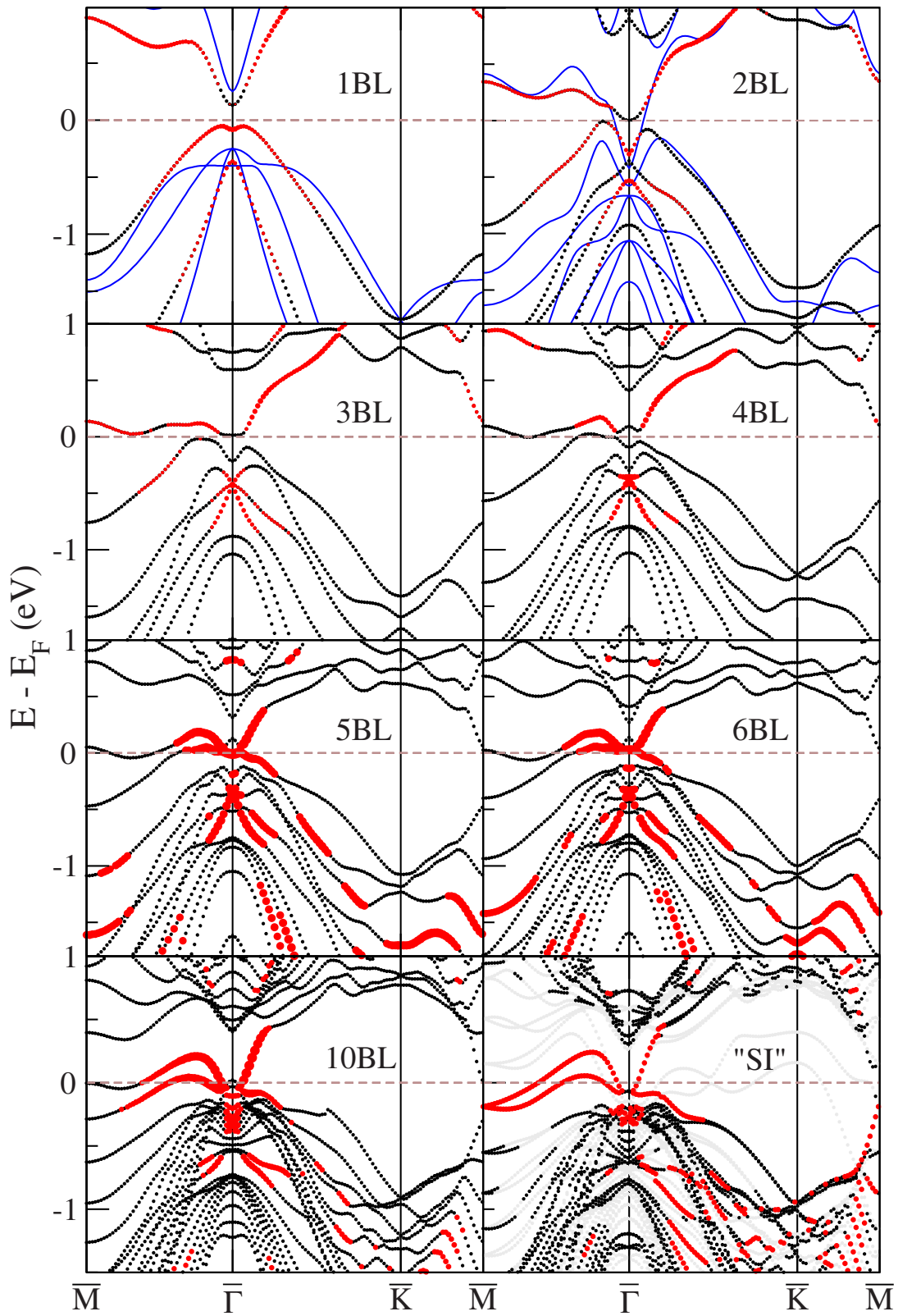


FIGURE 4.5: Band structures of Bi(111) films with one to six bilayer thickness as compared to a thicker (ten BL) film and a semi-infinite ("SI") crystal surface. Taken from [61].

To get a proper simulation of a Bi(111) film, a good saturation is necessary. A common procedure is to keep the bottom layers fixed in the ideal bulk position and use hydrogen termination for simulating the connection to the crystal like it was done for the In-nanowires on silicon in Chapter 3. Here, each dangling bond of the bottom side of the slab is saturated by hydrogen, and like in most situations a good description is achieved. However, in the case of the Bi(111) surface this approach leads to some unwanted features in the band structure. In the lower right corner of Figure 4.5 the band structure of a so-called “semi-infinite” (“SI”) crystal is shown. It consists of 22 bismuth layers with hydrogen termination. The bands resulting from the hydrogen atoms are displayed in grey. Two of them are directly located at the Fermi energy which leads in general to a false description of the structure. Another feature arising from the hydrogen atoms is the band crossing of every second band at the M point which does not appear without hydrogen termination. This point remains undiscussed in the paper, although the same authors have shown earlier that they get the best agreement of experiment and theory for a Bi(001) surface if they use freestanding films without termination but with space-inversion symmetry [110]. Naturally, one would believe that when going to the surface the space-inversion symmetry of the bismuth bulk is broken which should lead to a disappearance of the spin degeneracy. In the experiment this tends to become even more expected because the bismuth films are asymmetric with one side exposed to the vacuum and the other side to the silicon. But the opposite could be shown by Hirahara et al. in their paper [110]. Surprisingly, the breakdown of the inversion symmetry does not have any effect on the states around the M point.

We follow the same path and use a bismuth slab consisting of ten bilayers where the inner six bilayers are kept fixed at their ideal (PBE) bulk position and the outer layers can relax freely. Like this we can reproduce the band structure calculated in Figure 3 (a) of [109] where the authors used as well a symmetric 10 bilayer slab. With this (well-converged) slab, we can investigate the changes in the interlayer distances in comparison with the PBE bulk calculations. At the (111) surface, only the first bilayer is mainly affected. Both, the short and long interlayer distances are increased by 1.9% to $d_{12} = 1.60 \text{ \AA}$ and by 2.4% to $d_{23} = 2.53 \text{ \AA}$. All other distances differ only slightly ($< 1.5\%$).

When an impurity is incorporated, as we will see later (cf. Section 4.2), inbetween the first bilayer, the single layers of the first bilayer make room for the new atom.

Compared to the clean Bi(111) surface, the distance is increased by more than 12% to $d_{12} = 1.88 \text{ \AA}$. However, the distance between the first two bilayers is decreased by 13% to $d_{23} = 2.20 \text{ \AA}$ and the distance between the second and third (fixed at bulk positions) bilayer becomes even more bulk-like with $d_{45} = 2.37 \text{ \AA}$.

A detailed analysis of this symmetric slab, at first for the clean surface, is illustrated in Figure 4.6 (a-e). We gradually increased the number of bilayers from five to ten. The outer two bilayers are always free to relax and the inner layers are kept fixed at their ideal bulk position. Angle-resolved photoemission spectroscopy (ARPES) plots around the Fermi energy always show an electron pocket followed by a hole pocket and then again a second electron pocket [61, 111–113]. This can only be accurately reproduced if we use at least a symmetric slab of eight layers (d) where the highest and lowest two bilayers can freely relax and the inner four bilayers are kept fixed. A reduction of layers leads to a separation of the bands at the Fermi level and therefore a disappearance of the electron and hole pockets. This becomes even more clear when simulating the Fermi surface. Figure 4.7 displays a comparison of a symmetric five (a) and a symmetric nine bilayer (b) slab. The five-bilayer structure shows only the inner electron pocket in form of a hexagon. The outer lying hole and the second electron pocket, which are confirmed by a lot of experiments, are only reproduced with more bilayers.

Additionally, Figure 4.6 (f) shows a comparison between the scalar-relativistic band structure, i.e. SOC is not included, and the relativistic band structure of a symmetric slab with ten bilayers. Although some bands can be retrieved, especially near the M point, the band structure experiences dramatic changes. Around the Γ point the bands are degenerate. This degeneration is lifted in the SOC including band structure. Again the Fermi surface serves as a good indicator for differences, see Figure 4.7 (c). In the scalar-relativistic case, we can find a large electron pocket in the center which, because of the band degeneration around Γ , touches the outerlying hole pockets in the direction $\Gamma - K$. The electron pockets near the M point are not closed which is in contrast to the SOC-including Fermi surface. The large differences in the band structure and Fermi surface prove again the necessity of SOC in all electronic calculations regarding bismuth.

Besides the number of layers, the question of the number of fixed layers arises. For the above analysis, the outer two bilayers of the top and bottom surface were free to relax and the inner bilayers were kept fixed. To see, if it is sufficient to let only the outer two bilayers relax, additional tests were performed for a ten-bilayer slab

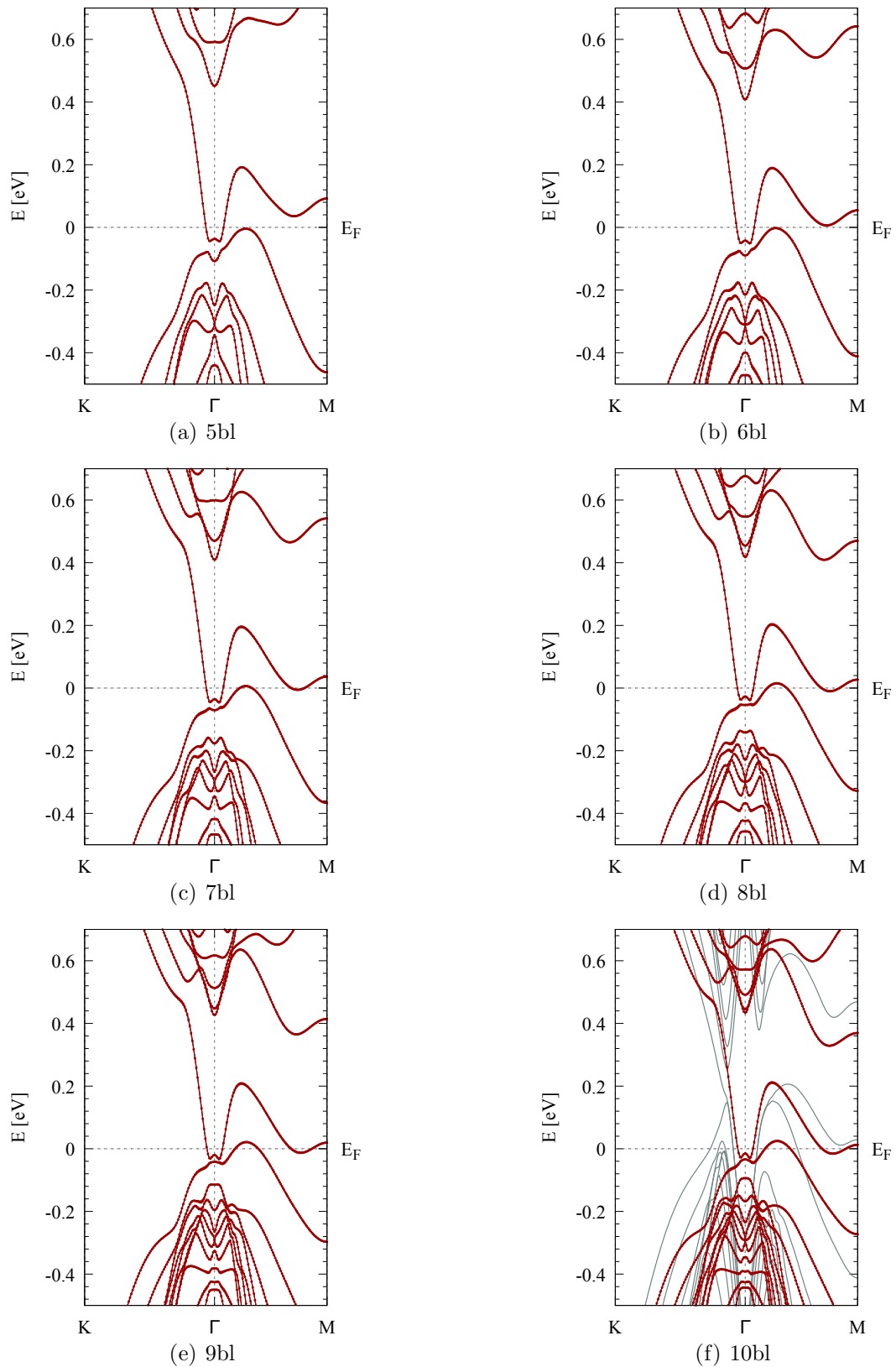


FIGURE 4.6: Band structures of the clean bismuth (111) surface for symmetric slabs with different numbers of bilayers. To get reproduce all typical features (i.e. the electron and hole pockets) a symmetric slab of at least eight bilayers is needed. Additionally, the scalar-relativistic band structure (i.e. SOC is neglected) for the 10-bilayer-slab is shown in grey.

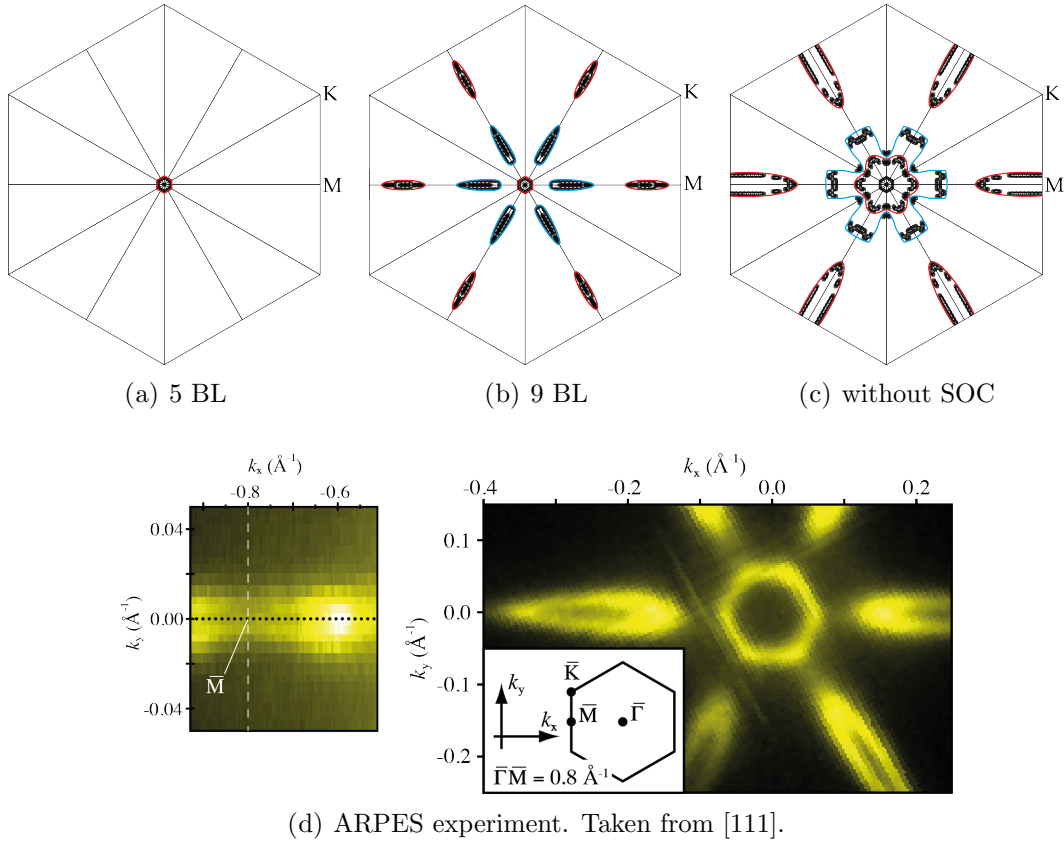


FIGURE 4.7: 2D plot of the Fermi surface for the clean Bi(111). A five bilayer slab (a) only shows the central hexagonal electron pocket (a). A slab with nine bilayers (b) reproduces all features seen in the experiment (d), an electron pocket followed by a hole pocket and then again an electron pocket. The calculation without SOC (c) looks totally different and cannot reproduce the experiment at all.

where different numbers (from none to eight) of bilayers can relax. The system where all layers resp. eight layers are kept fixed, i.e. the truncated bulk, is artificial and likely will not occur in nature.

First, we look at the total energy. As expected, the more layers are free to relax, the more energetically favorable is the system. The difference between two and eight free bilayers amounts to 16.5 meV. This is also visible in the band structure illustrated in Figure 4.8. The overall shape of the bandstructure is the same for all systems. But at the Γ point the differences become visible. For the structure with eight free bilayers (purple), i.e. four on both sides of the slab, the energy lies even above the Fermi energy and intersects the Fermi level at $\pm 0.1 \text{ \AA}^{-1}$ around Γ , a feature not seen in any other theoretical or experimental obtained band structure [109, 114, 115]. This is especially visible in the paper of Ast and Höchst [115] which includes ARPES measurements of the Bi(111) surface. The resulting Fermi surface shows no signs of bands below $k_F = 0.05 \text{ \AA}^{-1}$ around Γ (Figure 1 in [115]). Hence, it is safe to assume that two fixed bilayers are too few. All other Fermi

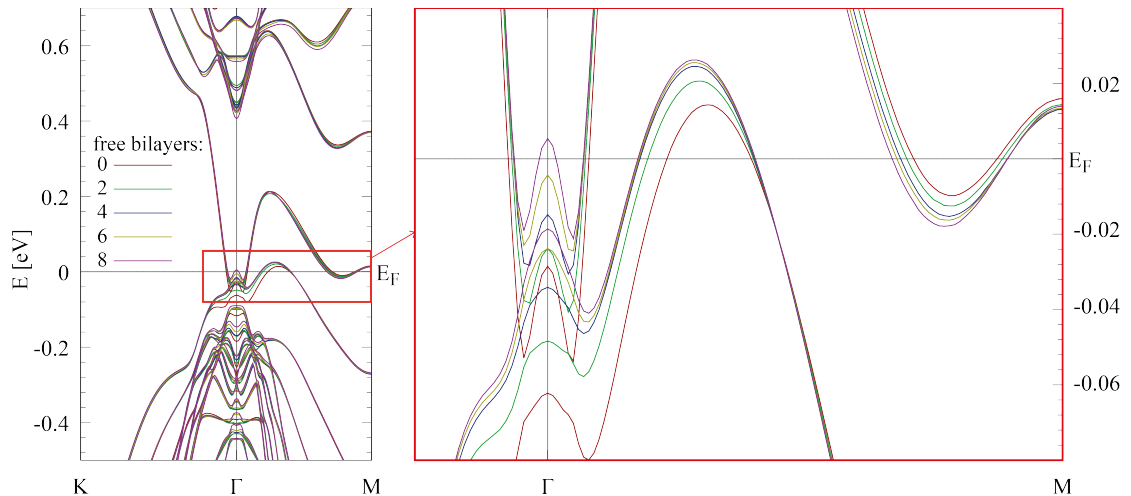


FIGURE 4.8: Band structure of a symmetric ten bilayer Bi(111). A different number of bilayers (from none to eight) are free to relax, the remaining bilayers in the middle of the slab are kept fixed at their ideal PBE bulk positions.

level crossings for eight (purple), six (yellow) and four (blue) free bilayers lie more or less on top of each other. The two structures with the fewest free bilayers (green and red) show clear discrepancies for the Fermi crossing at 0.15 \AA^{-1} . Obviously, the uppermost two bilayers of the bismuth (111) surface are mainly responsible for the behavior in the region of the Fermi energy.

The remaining parts of this chapter deal with the incorporation of adatoms into the bismuth (111) surface. Figure 4.9 (a-e) presents the band structure of a cobalt-monolayer doped bismuth (111) surface for different numbers of layers. Again, a symmetric slab is used and the structures contain two Co atoms on both side of the slab. All Co atoms are incorporated into equivalent, highly symmetric sub-surface site within the uppermost bilayer, cf. Figure 4.15 in Subsection 4.2.4. A detailed discussion of this characteristic position will follow in Section 4.2. We briefly note here, that this δ -doping Co layer provides the most stable configuration of Co adsorbates. For finding the best modelling, we use the (1×1) unit cell. A Co-doped (1×1) cell corresponds to a δ -doped surface, i.e. a Co monolayer within the first bismuth bilayer. Subsection 4.2.4 intensively deals with this system.

The doped surface, cf. Subsection 4.2.4, is more stable against layer-reduction than the clean bismuth surface as can be seen in Figure 4.9. Fewer layers lead to a lifting of the band structure by around 40 meV. Although this is not a small value, the overall form of the band structure and especially the Fermi level crossing of two bands (in the following called B_1 and B_2) remains. This is in contrast to the clean bismuth (111) surface where in total four crossing points vanish for five and six bilayers. For the δ -doped surface all crossings can be reproduced even with five

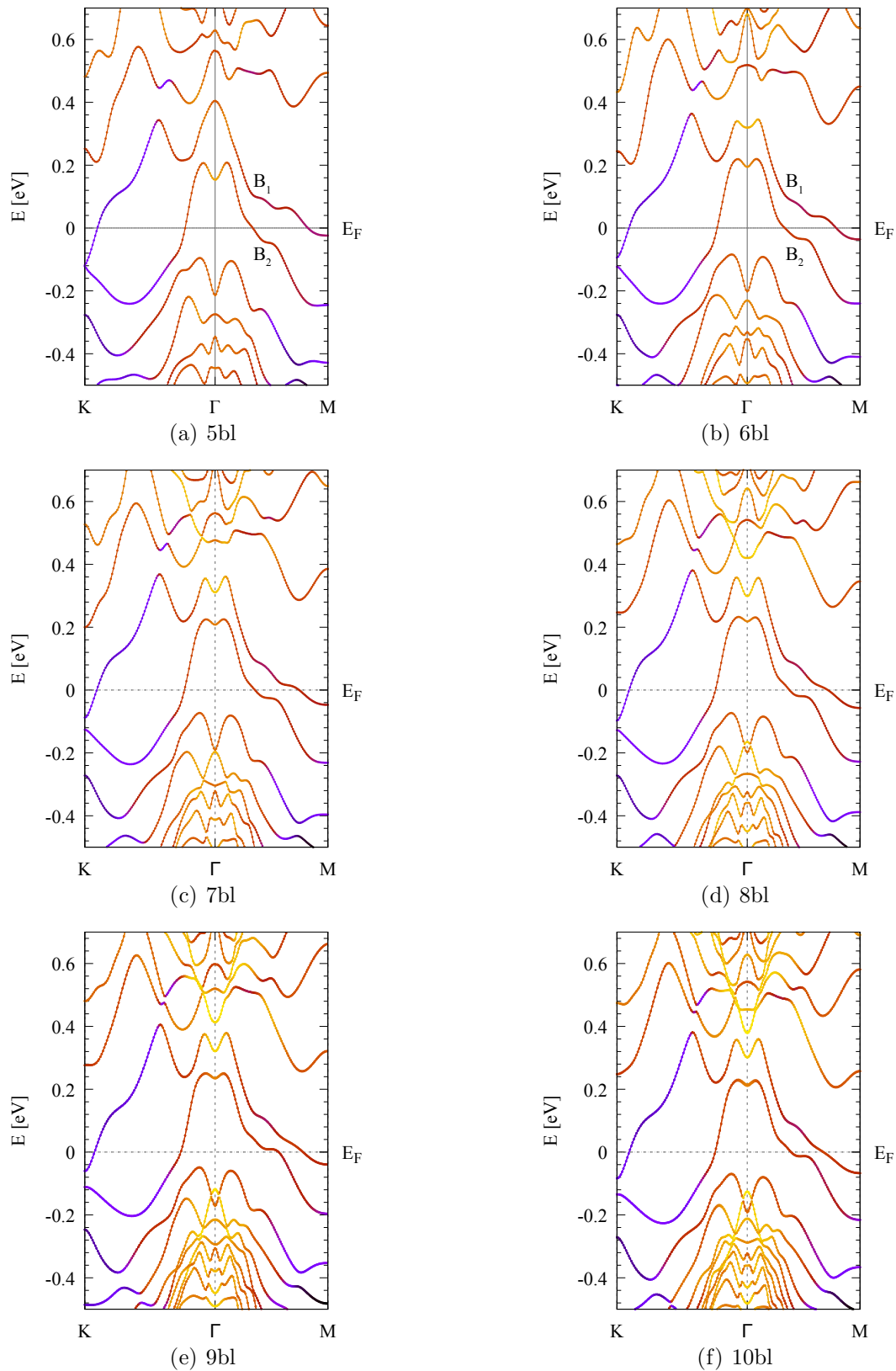


FIGURE 4.9: Band structures of the δ -doped bismuth (111) surface for symmetric slabs with different numbers of bilayers. Blue denotes high Co contribution whereas yellow corresponds to high Bi contribution. Already a symmetric slab with five bilayers is sufficient to get converged bands near the Fermi energy.

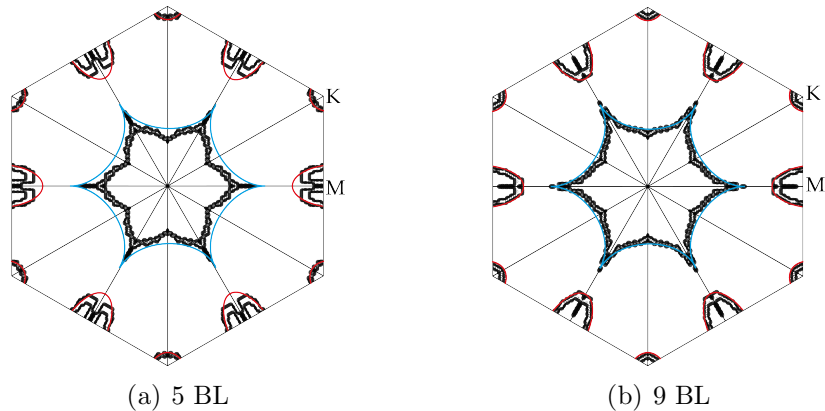


FIGURE 4.10: 2D plot of the Fermi surfaces for the δ -doped Bi(111) surface. The five bilayer slab (a) already reproduces the features of the nine bilayer slab (b), a hole pocket followed by electron pockets at the K and M point. B_1 and B_2 are the two bands which cross the Fermi level and show the biggest changes when going from a five bilayer slab to one with more bilayers.

bilayers. Thus, the Fermi surface, a little thinned out, looks similar for five or nine bilayers, cf. Figure 4.10. The most visible discrepancy between the five-bilayer structure and the others is the loss of the double feature of B_1 at the Γ point. The peak of the band is around 70 meV higher than for the more-layer systems. The difference between B_1 and B_2 amounts to nearly 280 meV, more than double the value as for the other systems. Furthermore, B_1 at the Γ point has both Co and Bi contributions whereas B_2 has only Bi contributions. This is opposed to the other systems where B_1 is a bismuth band and B_2 has contributions from both atomic species. For all other bands and k -points the occupation of the bands stays the same. This is due to the additional bands that come with extra layers. They hybridize with the other bands and thus cause the double feature and the different occupation of the bands B_1 and B_2 . Still, five layers already reproduce all features at the Fermi energy within a few meV. The magnetic moment, another critical parameter for our system, is stable against changes in the number of bilayers. With around $1 \mu_B$ it is the same for all tested systems.

So far, the δ -doping layer awaits experimental realisation. In the experiments presented in the following chapter, relatively low densities of cobalt (≈ 0.005 atoms/(1×1) unit cell) are used. The QUANTUM ESPRESSO package [16] used for all theoretical calculations works with periodic boundary conditions. Hence, for a totally correct description of the experimental occurrences, one would need a (14×14) unit cell. This is definitively not calculable, especially when spin-orbit coupling is included. We worked out that a (4×4) supercell is enough to exclude interactions between the impurity atoms in the periodic supercells. Three bilayers can be used for the

structural description, but for the electronic description (e.g. for band structures) a symmetric slab with at least five bilayers should be used. Unfortunately, it is not possible to investigate the number of layers for low impurity densities as everything above five bilayers it appears is too computationally demanding for the (4×4) cell.

4.2 Adatom incorporation into the Bi(111) surface

Most of the results in this chapter can be found in the related publications:

C. Klein, N. J. Vollmers, U. Gerstmann, P. Zahl, D. Lükermann, G. Jnawali, H. Pfnür, C. Tegenkamp, P. Sutter, W.G. Schmidt and M. Horn-von Hoegen
Barrier-free subsurface incorporation of 3d metal atoms into Bi(111) films
Physical Review **B** 91, 195441 (2015)

N.J. Vollmers, C. Klein, M. Horn-von Hoegen, C. Tegenkamp, H. Pfnür, W.G. Schmidt and U. Gerstmann
Bi(111) surface δ -doping by transition metal atoms
to be submitted (2016)

Some very recent results will contribute to a discussion of magnetotransport in a forthcoming paper where experiments are performed by the groups of Prof Pfnür and Prof Tegenkamp from the Leibniz-University in Hannover.

The electron transport in 2D surface electron systems such as the Bi(111) surface, can be influenced by individual scatterers [103, 112, 116, 117]. For example, the adsorption of bismuth itself on the Bi(111) surface leads to an increase in the resistance [103]. Controlled doping of the near-surface region is not uncommon for Bi₂Se₃ and Bi₂Te₃ [118–120]. Here, Fe is used as a dopant and, through thermally activated in-diffusion, occupies different interstitial or substitutional positions [119]. In this part of the thesis, the incorporation of individual impurity atoms into the bismuth (111) surface is shown. The related experiments were done by the group of Prof Horn-von Hoegen from the University of Duisburg-Essen and will not be discussed in much detail. Further information can be found in the recent doctorate thesis of C. Klein [106] and in the related publications [121, 122].

4.2.1 Experiment

The experiments were done using ultrastable low-temperature scanning tunneling microscopy (LT-STM). The very low base temperature of 5 K allows for a good comparison with the theoretical results that usually simulate 0 K-conditions. Figure 4.11 (a₁)-(a₃) show scanning tunneling microscopy (STM) micrographs in constant current mode after deposition of about 0.005 ML of the transition metal (TM) impurities Fe, Co, and Ni (with 1 ML = 5.6 atoms/nm²). Eye-catching is immediately that each impurity is surrounded by a similar threefold pattern.

Cobalt was used to study these pattern in more detail. At a bias voltage of $U_{\text{bias}} = +2.0 \text{ V}$ the bismuth surface looks as if nothing happened, cf. Figure 4.11 (b₁). With 1) to 4) structures of unknown origin are labeled. If the bias voltage is reduced to a value close to the Fermi level, $U_{\text{bias}} = 1 \text{ mV}$, the structures 1) to 4) are still visible, cf. Figure 4.11 (b₂). Additionally, extended pattern with threefold symmetry appear. They all have the same orientation, shape and size. As we will see later, the number of these pattern scales with the Co density which leads to the assumption that every pattern represents one Co atom.

In Figure 4.11 (c₁) - (c₃) and (d₁) - (d₃) one can see the STM pattern of a single Co atom for different bias voltages in higher resolution. The pattern is not visible at bias voltages of $\pm 2 \text{ V}$ but at voltages close to the Fermi energy. In comparison with the adsorption of a bismuth atom whose STM picture results in a bright spot visible over a broad range of bias voltages [103, 106], it seems that there are no morphological changes in the bismuth surface when cobalt is deposited. The Co atoms are incorporated within the surface and not on top of it. A similar case can be, for example, found in the publication of West et al. [119] where Fe is predominantly incorporated substitutionally in the Bi₂Te₃ (111) surface. Here too, the corresponding STM pictures have a threefold symmetry.

Before we come back to the theoretical point of view, an additional experiment performed by the University of Duisburg-Essen is presented which investigates what happens when the density of cobalt atoms is increased. Figure 4.12 (a-d) shows a row of STM pictures where gradually more Co was inserted into the bismuth surface. The number of Co pattern N scales with the Co density and increases from 229 to around 4000 per 100 nm². In Figure 4.13 dots illustrate the positions of the threefold pattern with each dot representing one pattern. The newly appearing pattern (red) do not seem to influence the ones from the last deposition step (black) which do not change their position, but stay where

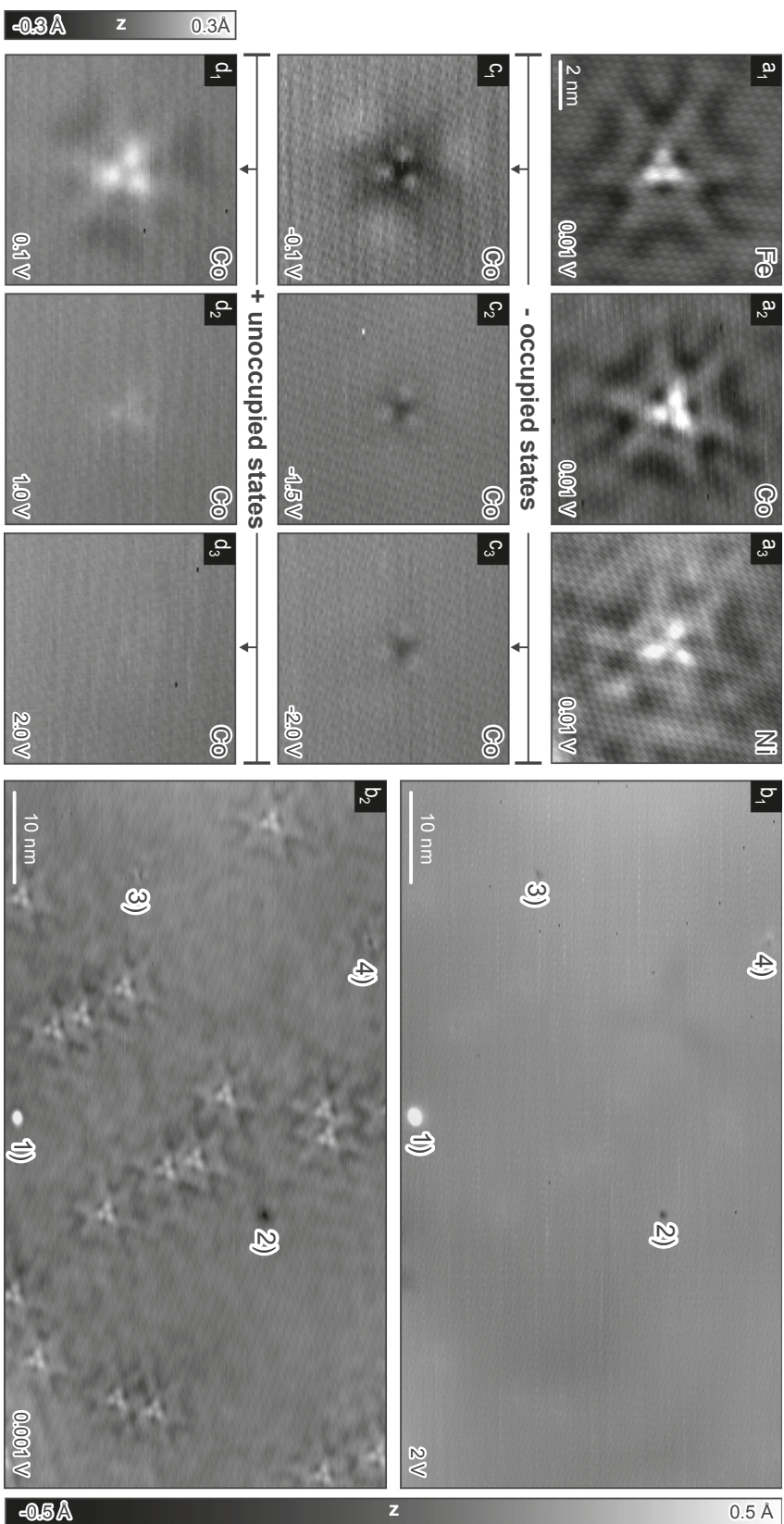


FIGURE 4.11: (a₁ - a₃): STM pictures of the impurity atoms Fe, Co, and Ni deposited onto the Bi(111) surface. (b₁) and (b₂): STM image of single Co impurities on a 20 nm Bi(111) film in constant current mode and identical z scale (-0.5 to 0.5 Å), taken under different conditions: (b₁) $I = 0.05$ nA, $U_{\text{Bias}} = 2$ V, and (b₂) $I = 0.05$ nA, $U_{\text{Bias}} = 1$ mV. 1) to 4) indicate other impurities or defects whose origin is not known. (c₁ - c₃) and (d₁ - d₃): STM pictures of a single Co impurity for different bias voltages ranging from -2 to +2 V. The z scale (-0.3 to 0.3 Å) is identical in all the images (a), (c) and (d). Taken from own publication [121].

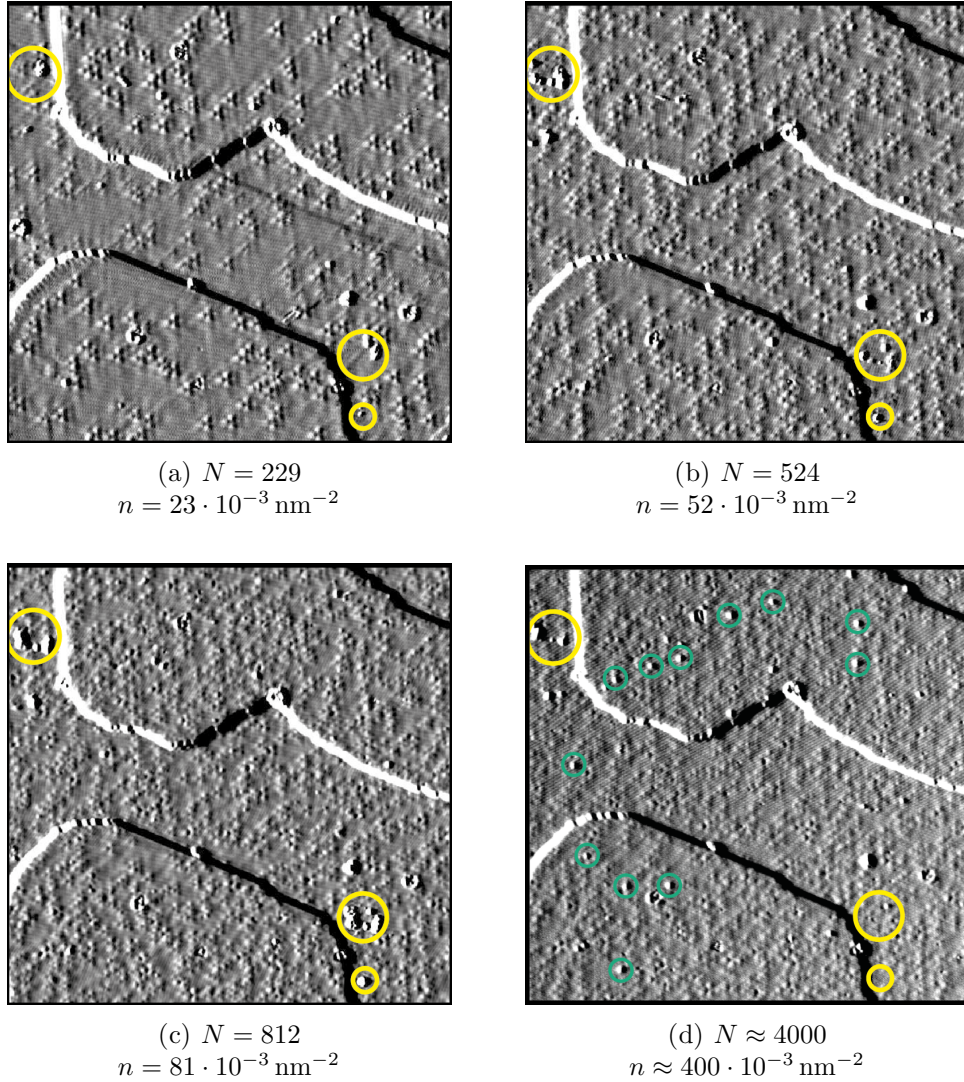


FIGURE 4.12: STM constant current images from Co adsorbed beneath a Bi(111) surface taken at 5 K, $U_{\text{Bias}} = 50 \text{ mV}$, and $I_{\text{tunnel}} = 50 \text{ pA}$. Field of view is $100 \times 100 \text{ nm}$. Density of the threefold pattern ranges from $23 \cdot 10^{-3} \text{ nm}^{-2}$ (a) to $81 \cdot 10^{-3} \text{ nm}^{-2}$ (c) and roughly $400 \cdot 10^{-3} \text{ nm}^{-2}$ (d). The yellow circles show example regions where the particle clusters first increase (a-c), but at the end decrease (d) with increasing density. Simultaneously, additional spots of identical shape (green circles) appear (d). Provided by the group of Prof Horn-von Hoegen from the University of Duisburg-Essen (see own future publication [122]).

they are. It is now clear that every threefold pattern represents one Co atom built-in somewhere within the surface at similar positions. But the Co atom can also form clusters as indicated by the yellow circles in Figure 4.12. They enlarge with increasing Co density (a-c). But if the density is increased by a further factor of five (d), they decrease again or even vanish completely. Although a possible contribution of bismuth atoms cannot be excluded, this indicates some kind of interaction between the cobalt atoms causing the clusters to fall apart. Additionally marked by the green circles are several new spots. It can be assumed

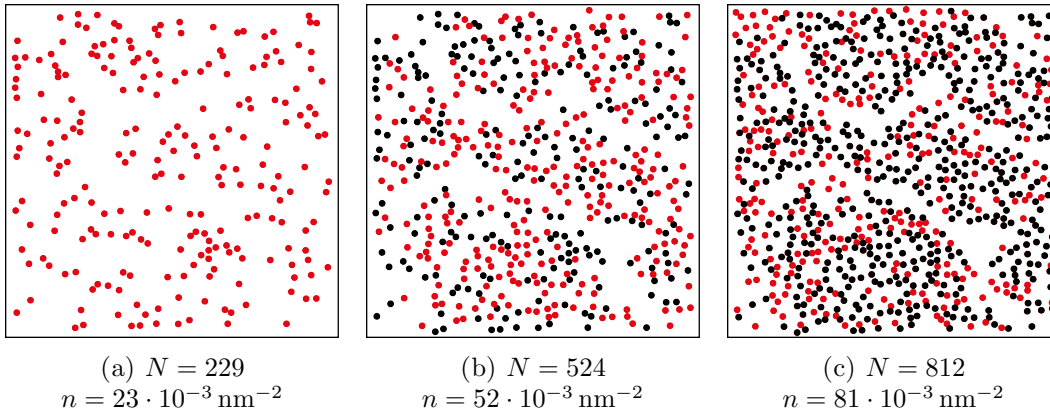


FIGURE 4.13: positions of the STM pattern from the experimental STM image of the Bi(111) surface, cf. Figure 4.12. Each dot represents one threefold shaped STM pattern. The density of the pattern ranges from $23 \cdot 10^{-3} \text{ nm}^{-2}$ (a) to $81 \cdot 10^{-3} \text{ nm}^{-2}$ (c). The newly appearing pattern are shown in red whereas the ones from the last deposition step are pictured in black. Interestingly, those seem not to be influenced by the new pattern and remain at their position. Provided by the group of Prof Horn-von Hoegen from the University of Duisburg-Essen (see own future publication [122]).

that these are the results of Co atoms staying ontop of the surface. Again, some involvement of bismuth is also possible.

4.2.2 DFT calculations

From the experimental STM images it can be suspected that all Co atoms are incorporated at identical subsurface sites leading all to the same typical threefold pattern. Furthermore, this incorporation seems to proceed without any thermal activation. By using density functional theory (DFT) calculations, we want to provide a solid ground for this hypothesis. As shown in the section before, relativistic effects have a large impact on the electronic structure of bismuth and have to be taken into account. However, for a structural relaxation, a scalar-relativistic description is sufficient. All further calculations such as magnetic moments were done with a multicomponent relativistic approach with noncollinear spin polarization as presented in Section 2.3 and implemented within the QUANTUM ESPRESSO package [16] which uses periodic boundary conditions. For an accurate description of the experimental conditions, it is necessary that the impurity atoms do not interfere with each other. This is approximately the case in a (4×4) unit cell. Still, the low experimental concentration of $0.005 \text{ atoms}/(1 \times 1) \text{ unit cell}$ is with $0.25 \text{ atoms}/(1 \times 1) \text{ unit cell}$ by far not achieved. But larger cells exceed our computational limits if bearing in mind the high number of \mathbf{k} -points ($6 \times 6 \times 1$ for the (4×4)

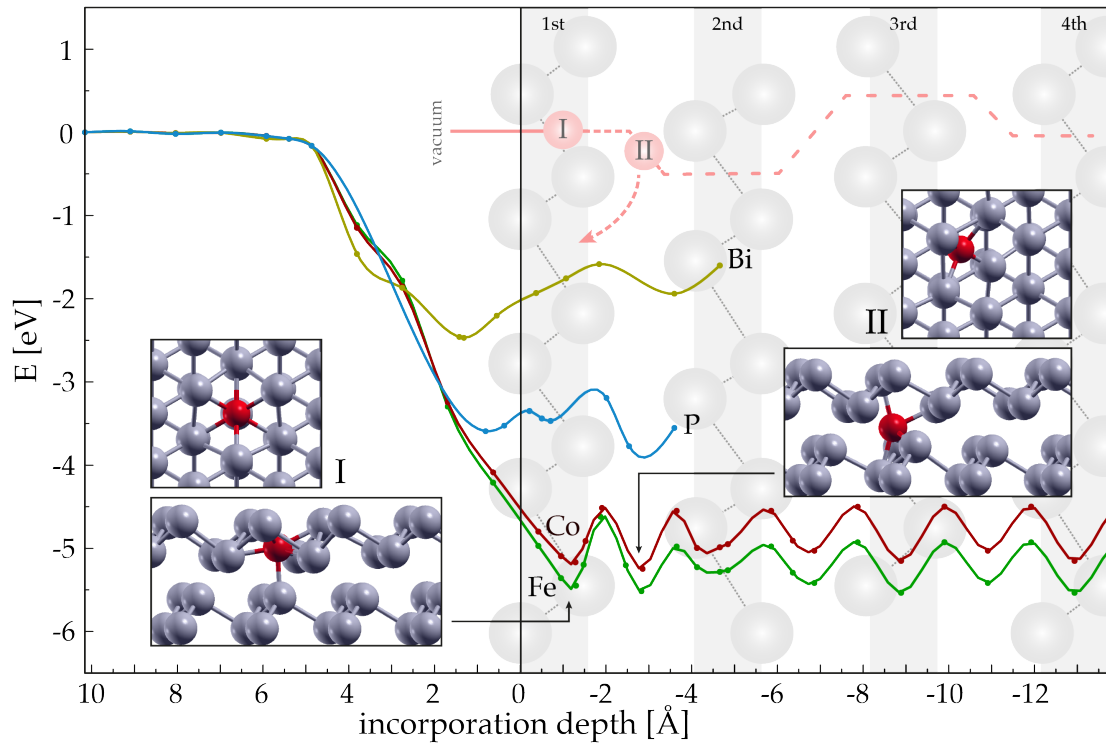


FIGURE 4.14: Total energy curve for different adatom positions and different atomic species (Fe, Co, P, and Bi), the microscopic structures of the first (I) and second minimum (II) and the schematic migration path for a $3d$ TM atom (here Co) into the Bi bulk (arrow: relaxation in interlayer position as requirement for lateral motion). Taken from own publication [121].

cell) and the high energy cutoff (90 Ry) also needed. All in all our (4×4) cells contain between 97 and 162 atoms.

4.2.3 *Barrier-free* subsurface incorporation of isolated $3d$ metal atoms into Bi(111) films

First of all, we want to find the global and local minima of our systems to predict the adsorption position of the adatoms. Figure 4.14 shows the reaction paths of various species of adsorbed atoms with respect to the energy of the adatom in the vacuum. These paths are calculated by keeping the z coordinate of the adatom fixed but allowing its lateral position and the Bi within the uppermost bilayers to relax. The nudged elastic band (NEB) approach is then used to explicitly determine the saddle points and corresponding energy barriers [123].

By closer examination of the energy curves, it can be seen that there are mainly two different positions where the adatom can be coordinated, on top of a Bi atom

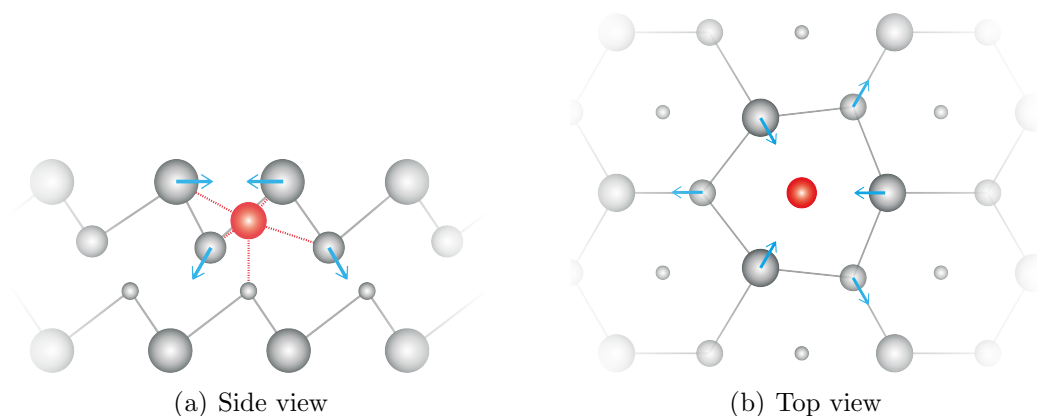


FIGURE 4.15: Schematic view of Co in Bi(111). Only one subsorbate positions is occupied. The Bi atoms of the first layer move closer to the Co but do not change height whereas the atoms of the second layer recede and move a little bit downwards.

of the first bilayer or within the first bilayer (marked with I in Fig. 4.14). More minima, which are energetically nearly degenerate, can be found deeper in surface (marked with II in Fig. 4.14).

Whereas Bi and P have a first minimum on top of the bismuth surface, Fe, Co and, as we will see later, all the other $3d$ TMs, go *barrier-free* into minimum I, without any thermal activation required. This *barrier-free* subsorption can be understood as a mix of two processes. First, the TM atom forms a planar configuration with the three Bi atoms of the uppermost Bi layer. At the same time, the $3d$ electrons are polarized by the second bismuth layer and the impurity is dragged further into the first bilayer. Here it stays and forms six bonds to the first-bilayer-ligands as well as one bond to the second-bilayer-atom right below. The outcome is a highly symmetric position which preserves the threefold symmetry set by the bismuth surface. Such high coordination is not untypical for $3d$ TMs and is for example known from Co in $\text{CoSi}_2/\text{Si}(111)$ [124]. Figure 4.15 presents a schematic view of this position. Blue arrows indicate the relaxation of the bismuth atoms surrounding the impurity. The length of the Bi-Bi bonds around the subsorbate increases by 2% for Sc up to 6% for Cr. This can be mainly attributed to the downwards relaxation of the second layer atoms. The first layer atoms move closer towards the impurity but do not change their height and the surface remains smooth as already indicated by the experiments.

The threefold symmetry of the highly symmetric incorporation site is also visible in the resulting STM picture shown in Figure 4.16 (a). The three bright spots, which form a triangle, were already seen in the experiment (cf. Figure 4.11). Such good agreement vanishes if we look at the simulated STM pictures for the minimum deeper in the surface (Figure 4.16 (b)). Directly at first glance, the

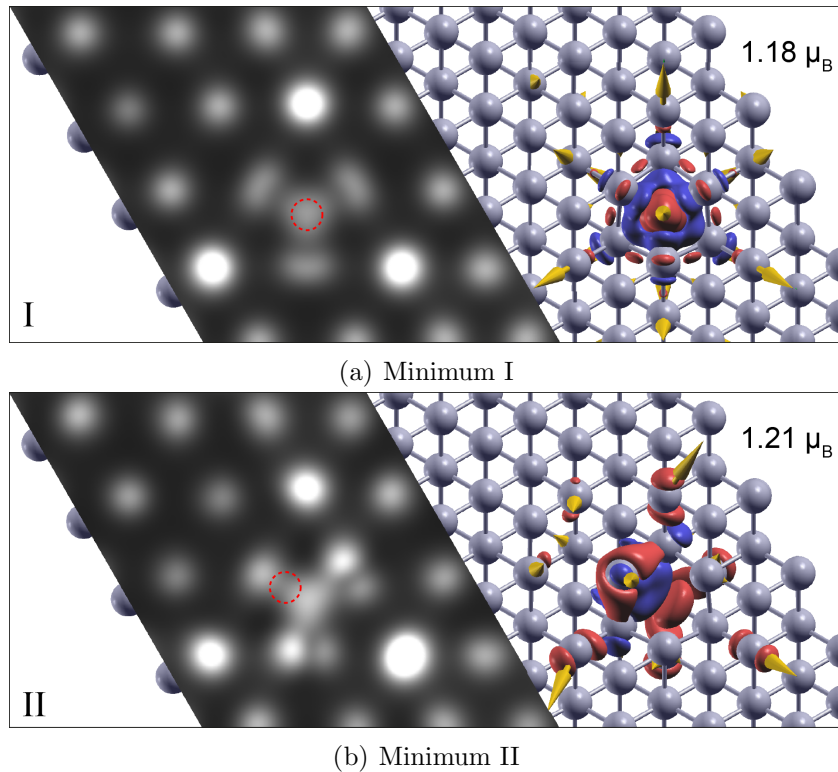


FIGURE 4.16: Calculated STM image for a Co (red circle) in the highly symmetric minimum I within the first Bi bilayer and in the asymmetric minimum II between the first two bilayers. The bias voltage is $U = 10$ mV. Co assumes a ferromagnetic configuration in both minima with the magnetic moments $1.18 \mu_B$ and $1.21 \mu_B$. Additionally, the magnetization density induced by the Co atom and the noncollinear spin orientation are displayed. Taken from own publication [121].

asymmetry of this position becomes clear. Although, there are three bright spots in the same distance as for minimum I. The center part is, however, very different and reveals two spots with similar intensity but only at two sides of the triangle. This feature is definitively not visible in the experiment and therefore one can exclude minimum II as the predominant incorporation site. Figure 4.16 (a) and (b) also show the magnetization density induced by the Co atom in minimum I and II as well as the noncollinear spin orientation (yellow arrows). Again, minimum I is the more symmetric structure. A lot of magnetization density is located at the Co atom and has the shape of a curvy triangle. For minimum II it becomes more obvious that the threefold symmetry, present in all experimental STM pictures, is lost. The magnetization density is still localized at the Co atom but shifted in the direction opposite to the lateral displacement of the Co. Yet, both minima have some similarities in the spin orientation. The spin localized at the impurity atom points in the direction of the surface normal whereas the spins localized at the bismuth atoms point away from the impurity.

The comparison of the STM pictures, the magnetization densities and the spin orientations confirm that the $3d$ TM atoms occupy position I which is by around 1.1 eV even more stable than any substitutional position. Together with the fact that this type of incorporation occurs *barrier-free*, this sets our finding apart from previous results, e.g. Fe in Bi_2Te_3 [119]. Migration into the deeper minima is improbable due to energy barriers of 0.7 eV (Co) up to 0.9 eV (Fe). If at position II, it is more likely for the $3d$ TM atom to move back into the first bilayer which requires activation energies below 0.5 eV instead of going deeper into the surface, thereby opening a possible mechanism for a lateral movement within the uppermost Bi bilayer (indicated by the red arrow in Figure 4.14).

Table 4.1 shows a comparison between the minimum on top of the surface and the one within the first bilayer for different atomic species. It is possible to put them into three groups:

- (1) **$3d$ TMs** with a partially filled d -shell have no minimum on top of the Bi surface (except for Sc but with a very low energy barrier of < 0.01 eV). This means that they go directly and *barrier-free* into the first bismuth bilayer and stay there. When the atom approaches the surface and interacts with the bismuth atoms, the $4s$ levels are energetically lifted and donate charge into the d orbitals. In the case of Co the occupation of the $4s$ states is reduced to 0.64

TABLE 4.1: Calculated adsorption and incorporation energies (in eV and relative to the respective free atom, metastable minima in brackets) for various third, fourth, and fifth row element adatoms at or in the Bi(111) surface together with energy barriers ΔE for the incorporation into the first Bi layer.

	Sc	Ti	V	Cr	Mn	Fe	Co	Ni	Cu	Zn
Top	(3.53)	—	—	—	—	—	—	—	—	0.49
1st BL	4.24	5.34	5.92	6.10	5.86	5.48	5.20	4.80	4.01	(0.26)
ΔE	< 0.01	—	—	—	—	—	—	—	—	0.27
								Pd	Ag	
Top								(2.81)	(1.71)	
1st BL								3.80	1.91	
ΔE								0.05	0.10	
	Bi	Pb						Pt	Au	
Top	2.60	2.61						(0.46)	(2.13)	
1st BL	(1.58)	(1.75)						1.54	2.34	
ΔE	0.89	0.24						0.15	0.17	

when 3 Å above the surface and to 0.47 electrons if incorporated. This results in the formation of highly coordinated σ bonds to the neighboring atoms.

- (2) **4d/5d and noble metals** tend to form higher bonds and thus it is not too much unfavorable to stay on top of the surface. Still, they just need to overcome a small energy barrier of up to 0.2 eV to get to their global minimum within the first bilayer.
- (3) **Atoms with no partially filled d -shell** cannot take advantage of the highly coordinated bonding position within the first Bi bilayer and have their global minimum on top of the surface. This is also true for rather small atoms like H or P which could be expected to slip through the first bilayer and are then stopped by the second-bilayer-atom.

The *barrier-free* incorporation is not only dependent on the existence of d -electrons of the adatom but also on the bond-length of the substrate. Using a single Bi(111) bilayer as a model system, we can modify its lattice constant and investigate the influence of strain on the incorporation. For Co, *barrier-free* incorporation occurs if the bilayer strain is between -5 % and +8 % of the ideal bond length. Otherwise either the lateral distance between the Bi atoms or the distance between two bismuth layers becomes too small. Hence, single Bi(111) bilayers on substrates should exhibit *barrier-free* incorporation of 3d TM atoms when the substrate's lattice constant is close to that of the Bi(111) surface. This applies for example to hexagonal BN (-2 %) and Bi₂Te₃ (-5 %). The famous and often investigated Bi₂Se₃ does not fall in this category. With a strain of 11 %, *barrier-free* incorporation is not possible, but thermal activation is required to get Co into the subsurface position.

4.2.4 Bi(111) surface δ -doping by transition metal atoms

In the last chapter, we have seen that 3d TMs take high symmetry positions if incorporated into the Bi(111) surface. Now, we want to investigate in more detail how the adatoms influence the structural and electronic properties of the bismuth surface, especially if more impurities come into play. Again, we pick Co as an example, but all results can be qualitatively transferred to the other 3d TMs.

In a first analysis, we look at pairs of Co atoms. The most stable configuration of Co pairs is given by direct subsorbate neighbors with a distance of 0.45 Å,

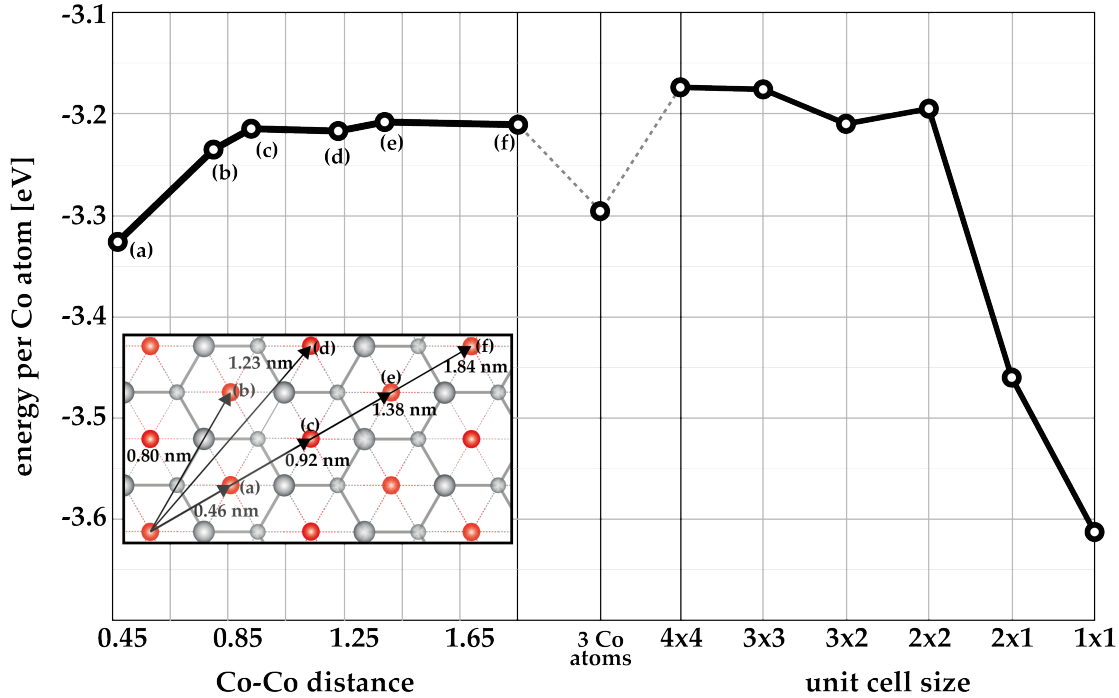


FIGURE 4.17: Binding energy E_B per Co atom for distant Co pairs (left), for a close arrangement of three Co atoms (middle) and for regular lattices depending on the cell size (right); decreasing cell size means increasing Co content. The exceptional stability of the subsurface TM layer, where each possible characteristic subsurface site is occupied, is manifested by a clear increase of $|E_B|$.

see (a) in Figure 4.17. More than 3.3 eV per Co atom can be gained by such an incorporation of two Co atoms. To understand this high stability we have to go back to the single incorporated Co atom: Here, the bismuth atoms of the first layer move closer to the Co and the second layer bismuth atoms recede (see Figure 4.15 in Subsection 4.2.3). Note, that the height of the first-layer bismuth atoms does not change, i.e. the surface remains smooth as already indicated in the experiments.

In the case of the nearest neighbor pair, the bismuth atoms of the first layer that separate the two Co atoms are simultaneously pulled in the direction of the two Co atoms. The acting forces cancel each other out and thus, instead of moving at all, the two bismuth atoms remain in their ideal (lateral) position. All other more distant pairs are energetically less favored. If a third Co atom is placed close to a stable pair (cf. “3 Co atoms” in Figure 4.17), i.e. three next-neighbor subsorbate positions are occupied, the binding energy per Co atom is nearly unaffected ($\Delta E \approx 0.03$ eV). Again, the bismuth neighbors shared by the Co atoms experience opposing forces and remain in their ideal lateral position. For the same reason is the highest possible density of Co atoms in subsurface

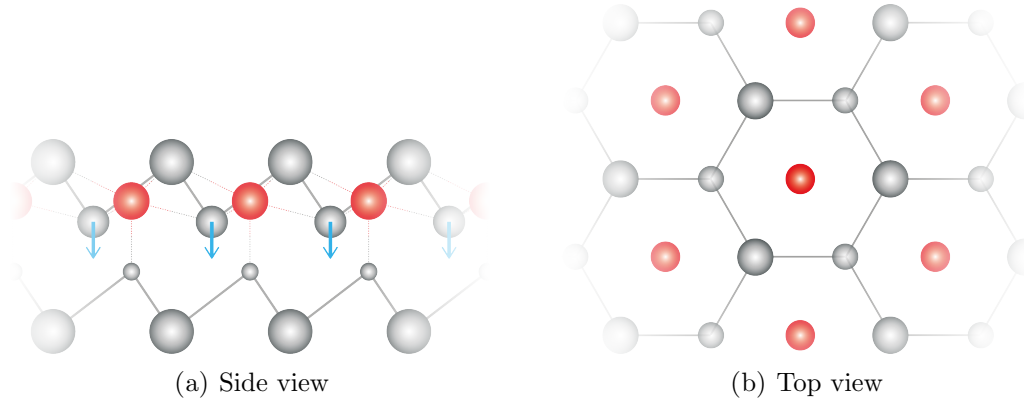


FIGURE 4.18: Schematic view of Co in Bi(111). Every subsorbate position is occupied. The Bi lattice shows no sign of lateral distortion and remains in its ideal (lateral) form (cf. (b) top view). Only the atoms of the second layer move a little bit to the second bilayer to reduce strain.

positions shown in Figure 4.18 the overall energetically most favorable. But here, the lateral positions of all bismuth atoms are unchanged. To reduce strain, the first bismuth bilayer is slightly shifted towards the second bilayer. This results in a very high stability of this δ -doped structure with one Co atom per (1×1) unit cell. In direct comparison with the lower density structures, e.g. one atom per (4×4) unit cell, round about 0.4 eV per atom can be gained. In general it holds that the higher the density the more energetically favorable is the system as can be seen in Figure 4.17. Note here, that for all possible incorporations of Co, be that isolated subsorbates, pairs or islands of subsorbates or the δ -doping layer, the surface topography does not change at all.

In contrast to the single Co impurity the non-collinear polarization of the magnetization (cf. Fig. 4.16 (a)) is revoked and all spins are aligned along the surface normal whereby the spins of the Co and of the Bi have opposing signs. Besides, the magnetic moment per Co atom reduces from $1.57 \mu_B$ to $1.0 \mu_B$. Still, the structure remains metallic as can be seen in the bandstructure: Figure 4.19 shows the bandstructure of the clean Bi(111) surface (grey) in comparison with bandstructure of the δ -doped surface (colored). The changes in the bands are extreme. This is due to a strong hybridization of the Co sublattice with the Bi host lattice (indicated by redish colors in Fig. 4.19). Only at the K point and around the Fermi energy and at the M point below -0.2 eV , i.e. regions where there are no bands of the clean Bi(111) surface, bands can be found which are mainly Co-related (dark blue). Those bands are spin-polarized and can be individually assigned to the spin channels. They are mainly responsible for the magnetic moment.

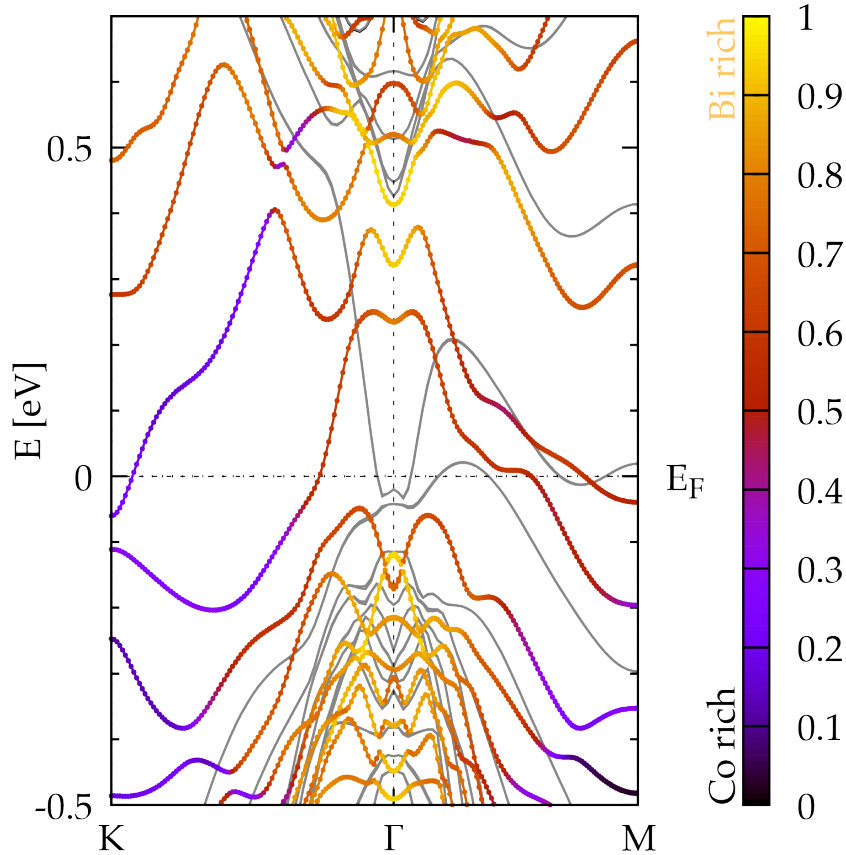


FIGURE 4.19: Relativistic bandstructure of the Co/Bi(111) surface with (1×1) δ -doping layer; colors (black/yellow) denote the Bi/Co contributions. For comparison, the bands of the ideal Bi(111) surface are shown in grey.

The changes, especially at the Fermi energy, become more clear when we look directly at the Fermi surface (Figure 4.20). (a) shows the Fermi surface of the clean Bi(111) surface. The typical electron pockets shown in red and hole pockets shown in blue are in correspondence with a lot of other publications, e.g. [61, 111–113]. The δ -doped surface has a central hole pocket around Γ and electron pockets at K and M . Whereas the hole pocket and the electron pocket near M are spin-unpolarized, we have a spin-down electron pocket near the K point. Because of the very different shape of the Fermi surface compared to the one of the clean bismuth surface, it should be possible to identify this system with angle-resolved photoemission spectroscopy (ARPES) measurements.

Since we started with trying to reproduce and explain STM images in the first place, it is only logical to simulate STM pictures for systems with a higher density of Co impurities. In Figure 4.21 STM pictures of different densities are compared with each other and with a pair of Co atoms from the experiment. The experimental twin structure (a) can be well reproduced by two Co atoms with a distance

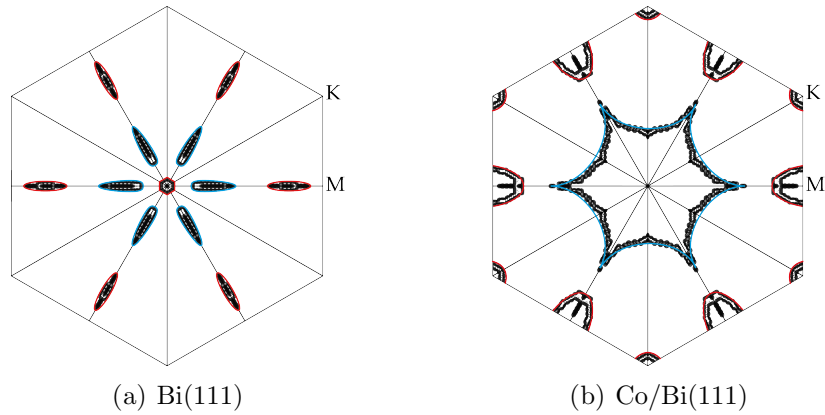


FIGURE 4.20: 2D plot of the Fermi surfaces for the clean and the δ -doped Bi(111) surface. The difference between both is clearly visible, especially because of the electron pocket near K which is only present in the case of the doped surface.

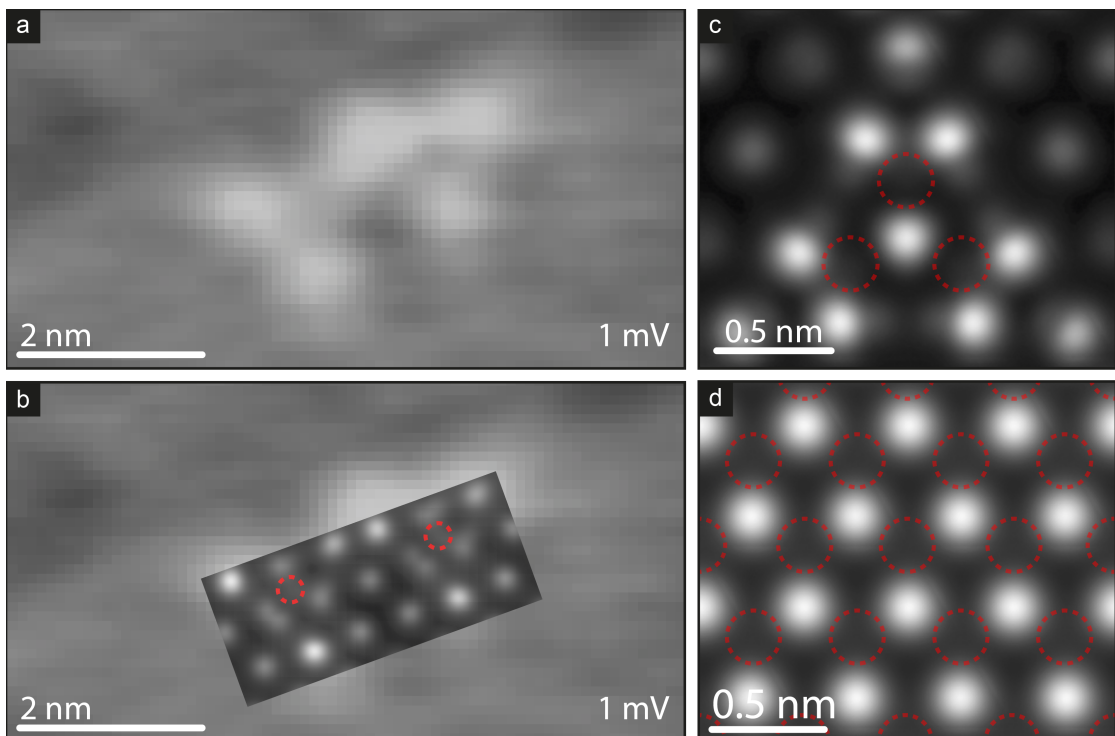


FIGURE 4.21: (a) Experimental STM image, $I = 0.05$ nA, $U_{\text{Bias}} = 1$ mV, of two Co impurities with a distance of about 1.5 nm (Taken from own publication [121]). (b) Corresponding calculation. (c) Calculated STM image for three Co atoms in next-neighbor subsorbate positions (red circles). (d) Calculated STM picture for δ -doped Co/Bi(111) surface.

of about 1.5 nm (b). At this distance the typical threefold pattern are still distinguishable from each other. This changes when the Co atoms come closer together, illustrated in (c). Here, three Co atoms are placed in next-neighbor subsorbate sites. The single pattern overlap and become slightly similar to the one of the clean bismuth (111) surface (cf. Figure 4.22). In the case of the δ -doping layer (d) the STM picture is exactly like the one without any impurity at all (Figure 4.22

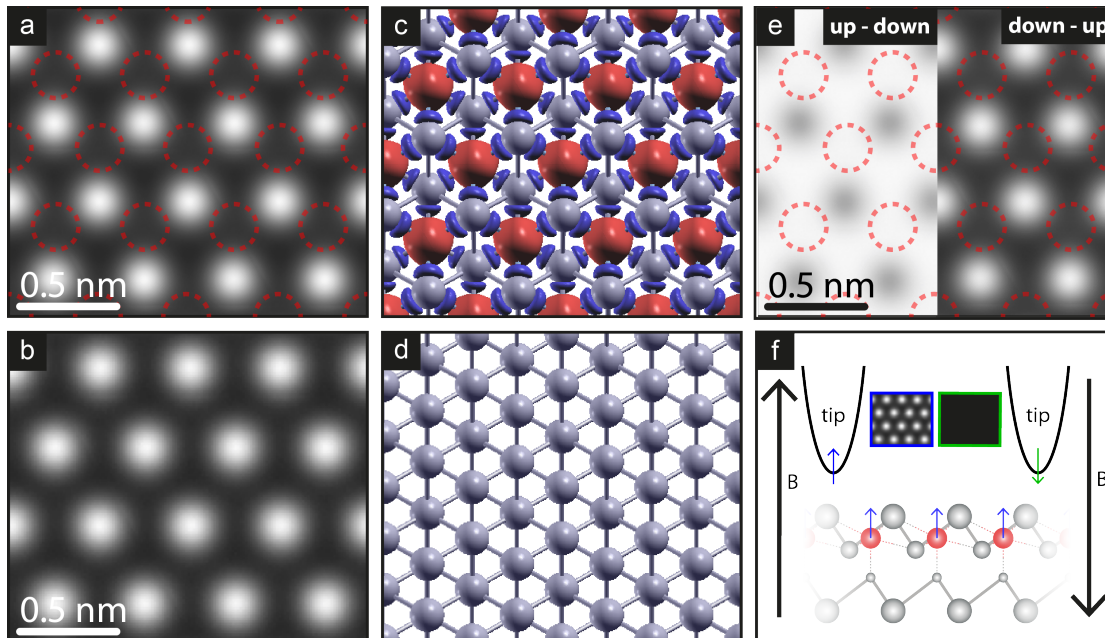


FIGURE 4.22: Comparison of the calculated STM pictures for (a) the δ -doped surface with red circles representing the Co atoms and (b) the clean surface. (c) and (d) show the corresponding magnetization density. (e) compares the spin-up and spin-down STM pictures. (f) illustrates a proposal for spin-polarized STM.

(a) and (b)). The Co atoms thus become STM-invisible. This means that such regions where every subsorbate position is occupied can easily be mistaken for regions with no subsorbates at all in STM measurements. However, the magnetization density is only present for the doped surface (Figure 4.22 (c) and (d)). The spin channels are clearly divided between the Co and the Bi atoms (Figure 4.22 (e)). As mentioned before, all spins are aligned along the surface normal with opposite signs for Co ($+z$) and Bi ($-z$) and with a way bigger magnitude for Co (Figure 4.22 (f)). This remains, even when an external magnetic field is applied in the $+z$ direction. Furthermore, the atomic spin directions do not change if we flip the direction of the external magnetic field. Hence, spin-polarized STM should be possible and result in clear different images for the two directions of the external magnetic field and thus in different images for the clean and the δ -doped bismuth (111) surface.

Even though the δ -doped surface is energetically favored it is useful to investigate which processes can happen during evaporation. We assume that a subsorbate site is already taken by a Co atom but a second atom is approaching from above. Different scenarios can now occur as visible in Figure 4.23. The red spheres demonstrate either the arriving Co atom or an already occupied subsorbate position. The red circle instead indicates a free next-neighbor subsorbate position. If the new Co

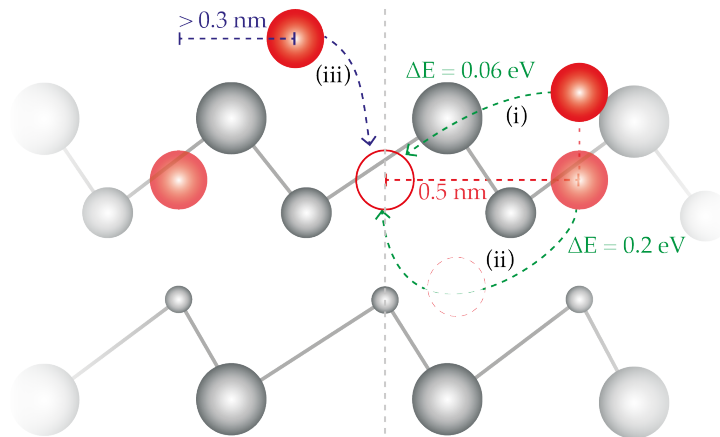


FIGURE 4.23: Side view of Co at the Bi(111) surface. Light red empty (filled) circles indicate possible (already occupied) positions. Dark red spheres show a new arriving Co atom: it can (i) be adsorbed on top of an already incorporated Co atom, overcome a barrier of 0.06 eV and move to the next free subsorbate position or (ii) push the incorporated Co atom into a neighboring free position. (iii) If the arriving Co atom has a distance of 0.3 nm or more from an incorporated one, it goes *barrier-free* into the next free subsorbate position.

atom has a distance of at least 0.3 nm from an already incorporated one, it goes *barrier-free* into the next free subsorbate position. Otherwise it stays on top of the other atom forming a Co-Co bond with a length of 2.5 Å similar to the one of Co bulk. Do more Co atoms arrive, they can form large clusters visible in the STM as big bright spots (cf. yellow circles in Fig. 4.12). However, a two-atomic cluster is not totally stable. Only a small energy barrier of 0.06 eV has to be overcome to cause the upper Co atom to move into the next subsorbate position. In another scenario, the upper atom pushes the incorporated atom in the next subsorbate position via the energetically nearly degenerate fivefold coordinated position presented in Subsection 4.2.3. Here, the energy barrier is at maximum 0.2 eV. The new arriving atom can now take the position of the pushed-away atom.

All in all, if we have a sample, grown at low-temperatures, with a high density of Co atoms, it is likely that they will either be incorporated at subsorbate positions or aggregate in clusters. However, a moderate temperature annealing should cause the Co atoms to move and rearrange. The clusters break and will fill up empty subsorbate sites around, thus forming δ -doped islands which should be stable even at room temperature.

Chapter 5

Summary

In the context of this work, a new approach for including relativistic effects in DFT calculations was developed, implemented in the QUANTUM ESPRESSO package and tested on different systems. We used a spinor approach where the spin-orbit coupling (SOC) enters in nonseparable form the nonlocal parts of scalar-relativistic pseudopotentials. The major benefit of this new method is the possibility to use the same pseudopotentials for scalar-relativistic and SO-including calculations. This ensures a good comparability between the two without having to bear in mind technical differences coming from different pseudopotentials. As first test systems we used the well-studied bismuth (111) bilayer which shows big differences in the band structure between the non-relativistic, the scalar-relativistic and the spin-orbit including or full-relativistic approach. With our method it was possible to reproduce the relativistic band structure within a few meV compared to the already implemented code [50] and the reference [61].

Furthermore, we used our approach to calculate the Rashba parameters for the Bi-related surface alloys Bi/Ag(111) and Bi/Cu(111). Those systems are known to have a large Rashba spin splitting [65, 66] and are therefore perfect reference systems. Our results were in very good agreement with experimental values and the ones from former theoretical work. Through our tests we were also able to see the high improvement regarding computational time. With the *reconstruction-only* approach the computational time was reduced by nearly two-thirds to 30% compared to the previously implemented full-relativistic approach of Andrea Dal Corso [50]. At the moment, the method works only for normconserving pseudopotentials, but we can expect a further reduction in computational costs if in the future ultrasoft pseudopotentials may be used.

After we could proof the usability and the huge reduction of computational time of our method, we used it to investigate relativistic effects of In nanowires that self-organize on the silicon (111) surface. We could show that both, the (4×1) and the (8×2) phase, exhibit a large and highly anisotropic Rashba effect. Striking is that the Rashba splitting does not appear at the Γ point, as it is the case with most other systems, but at the X point. Mainly the In-related bands are affected. To explain the band-dependent anisotropy, the orientation and population of the In $5p$ orbitals was analyzed. We could show for the room temperature (RT) phase that the two upper bands have a large p_y contribution resulting in a splitting perpendicular to the nanowires whereas the other two bands have more p_x contribution and thus a splitting along the wires. The new relativistic approach provides the possibility to turn on the spin-orbit coupling for specific atoms. By doing so, we were able to prove that mainly the outer indium atoms are responsible for the Rashba effect. The low temperature (LT) phase turned out to need a more complicated explanation for the Rashba anisotropy. The inner and outer indium atoms participate with same contributions as for the (4×1) phase but depending on the k -direction with parallel or opposite spin polarization. Hence, only a superposition of the bands where the spin-dependent splitting is either increased or canceled, can explain the strong Rashba anisotropy.

As a second class of investigated systems, modified bismuth surfaces were used. The bismuth (111) surface consists of different bilayers. As a first step, the best modelling was searched for because the electronic structure of the surface highly depends on the numbers of bilayers that are taken into account. We found that a symmetric slab of at least eight bilayers is necessary to reproduce the band structures and Fermi surfaces from theoretical and experimental work. The electronic structure was found to be more stable when adatoms come into play. Here, a symmetric slab with only five bilayers already shows all relevant features for the band structure in the region of the Fermi energy. The motivation for analyze the influence of adatoms came from the experimental group of Prof. Dr. Horn-von Hoegen. They deposited $3d$ TM on the Bi(111) surface and then examined the sample with STM. It was found that at a bias voltage near the Fermi energy threefold shaped pattern appear. The amount of these pattern corresponds to the amount of adatoms that were deposited. This lead to the assumption that every threefold pattern represents one impurity atom. With DFT calculations it was possible to reproduce the STM pictures and furthermore define the exact location of the adatom. It is incorporated sevenfoldly coordinated within the first Bi

bilayer directly above a Bi atom of the second bilayer. This incorporation even takes place *barrier-free*. Interestingly, the surface topography remains unchanged and only the Bi atoms around the impurity recede a little bit or move closer to the impurity. We used a wide range of different atomic species to perform total energy calculations for various positions. Only $3d$, $4d$, $5d$ and the noble metals have their global minimum within the first bilayer. But only the $3d$ TM occupy this position *barrier-free*. For the others, a small thermal activation is necessary to quit their local minimum on top. All atoms without a partially filled d -shell stay on top of the surface.

After finding this so-called subsorbate position, we went on to higher densities of subsorbates. As an example Co was chosen. Subsubstrate pairs in next-neighbor position turned out to be the energetically favored in contrast to pairs with higher distances. If we fill all possible subsorbate positions, i.e. one Co atom per 1×1 unit cell, we can gain around 0.5 eV compared to a single Co atom. A Co layer is built within the first bismuth bilayer. This δ -doping layer preserves the bismuth lattice, i.e. only the second-layer bismuth atoms decent slightly. This high stability explains the huge energy gain. Interestingly, the STM picture of the δ -doped surface looks exactly the same like the one from the clean bismuth (111) surface. Fortunately, the band structure and Fermi surface show very different characteristics. This means that ARPES can be used to distinguish the clean from the doped surface. Alongside δ -doped regions, we found that Co atoms can build clusters with one atom in a subsurface position and the others on top. However, those clusters are not stable and temperature annealing will likely cause the atoms to rearrange into neighboring subsurface positions. Consequently, a careful choice of the growth conditions paired with moderate temperature annealing should result in a δ -doping Co layer. Because of the similar incorporation behavior, δ -doping layers of other $3d$ TMs should be possible.

The combination of magnetic (Co) and non-magnetic (Bi) materials is very suitable for any kind of magnetic surface spectroscopy, as for example spin-polarized STM, X-ray magnetic circular dichroism (XMCD) or photo emission electron microscopy (PEEM).

Chapter 6

Outlook

Spin-orbit coupling (SOC) finds its way into the calculation of a wide range of properties. X-ray magnetic circular dichroism (XMCD), the difference of two X-ray absorption spectra, is just one example of where SOC becomes important and can change the outcome of a spectrum.

In X-ray absorption spectroscopy (XAS) or more specific X-ray absorption near edge structure (XANES), x-rays are used to liberate a core electron from the probe. The arising (element-specific) adsorption edge then gives information about the chemical environment of the sample, e.g. oxidation state, coordination, bonds etc. In general the XAS cross section is given by [125]

$$\sigma(\omega) = \frac{2\pi\omega}{I} \sum_f |M_{i \rightarrow f}|^2 \delta(E_f - E_i - \omega) \quad (6.1)$$

The XMCD cross section is then given by the difference of the XAS spectra for right- and left-circularly polarized light:

$$\sigma^{\text{XMCD}} = \sigma(\boldsymbol{\epsilon}) - \sigma(\boldsymbol{\epsilon}^*) \quad (6.2)$$

with $\boldsymbol{\epsilon} = \frac{1}{\sqrt{2}}(\mathbf{e}_x + i\mathbf{e}_y)$. XMCD is mostly applied to nonmagnetic surfaces with magnetic adatoms or vice versa.

The total cross section can be divided into different terms:

$$\sigma = \sigma_{D-D} + \sigma_{Q-Q} + \sigma_{D-Q} + \sigma_{D-SO1} + \sigma_{D-SO2} \quad (6.3)$$

σ_{D-D} , the dipole-dipole contribution is in most cases the dominating part of the spectrum and defines the overall shape. Sometimes, $s \rightarrow d$ transitions, the quadrupole term σ_{Q-Q} make some visible changes to the prepeak of the spectrum. The dipole-quadrupole term σ_{D-Q} has rarely a big influence to the total spectrum and is even zero for all systems with inversion symmetry. The just mentioned term are already known from absorption spectra (X-ray and optical). We want to focus on the SOC terms that arise explicitly from the inclusion of SOC, so far not discussed in literature:

$$\sigma_{D-SO1} = -2\pi^2\alpha^3 \sum_f \Im \left[\langle i | \boldsymbol{\epsilon}^* \cdot \mathbf{r} | f \rangle \langle f | \boldsymbol{\sigma} \cdot (\nabla V_{\text{scf}} \times \boldsymbol{\epsilon}) | i \rangle \right] \delta(E_f - E_i - \omega) \quad (6.4)$$

$$\sigma_{D-SO2} = -3\pi^2\omega^2\alpha^3 \sum_f \Im \left[\langle i | \boldsymbol{\epsilon}^* \cdot \mathbf{r} | f \rangle \langle f | \boldsymbol{\sigma} \cdot (\boldsymbol{\epsilon} \times \mathbf{r}) | i \rangle \right] \delta(E_f - E_i - \omega) \quad (6.5)$$

The official QUANTUM ESPRESSO code contains the possibility to calculate x-ray absorption spectra for the K -edge, i.e. exciting a $1s$ electron [125]. In the context of the previous work of C. Gougoussis and M. Calandra from the Pierre and Marie Curie University, as well as U. Gerstmann from the University of Paderborn, a first extension to XMCD was done for the σ_{D-D} , σ_{Q-Q} and σ_{D-Q} terms [127]. As part of the present doctorate, those implementations were improved and further extended, especially by including the σ_{D-SO2} term in combination with the new relativistic method presented in Section 2.3. As a test system, iron was used. The influence of the different terms is illustrated in Figure 6.1. The quadrupole-related contributions σ_{Q-Q} and σ_{D-Q} have small or no influence on the total spectrum. The dominating term is σ_{D-D} which already gets the shape of the experimental spectrum right. The quotient between the first positive peak and the first negative peak accounts to 1.2 in the experiment. For the σ_{D-D} term this quotient is with 0.7 too small. The σ_{Q-Q} makes things even worse by decreasing the first peak and leading to a quotient of 0.6. Thus, we need a term that influences both, the first and second peak. By adding the σ_{D-SO2} term to the spectrum the first peak increases a little bit whereas the absolute intensity of the second peak is decreased, i.e. the quotient gets better with a value of 1 but there is still a small error. This deviation can be ascribed to the not yet implemented term σ_{D-SO1} . Besides the inclusion of the still missing terms, an extension to L - and M -edges is planned and an evaluation of the so-called sum rules of XMCD spectra [128–131]. This will become useful for additional investigation of the bismuth surface. Related experiments are already carried out by the University of Hannover. For

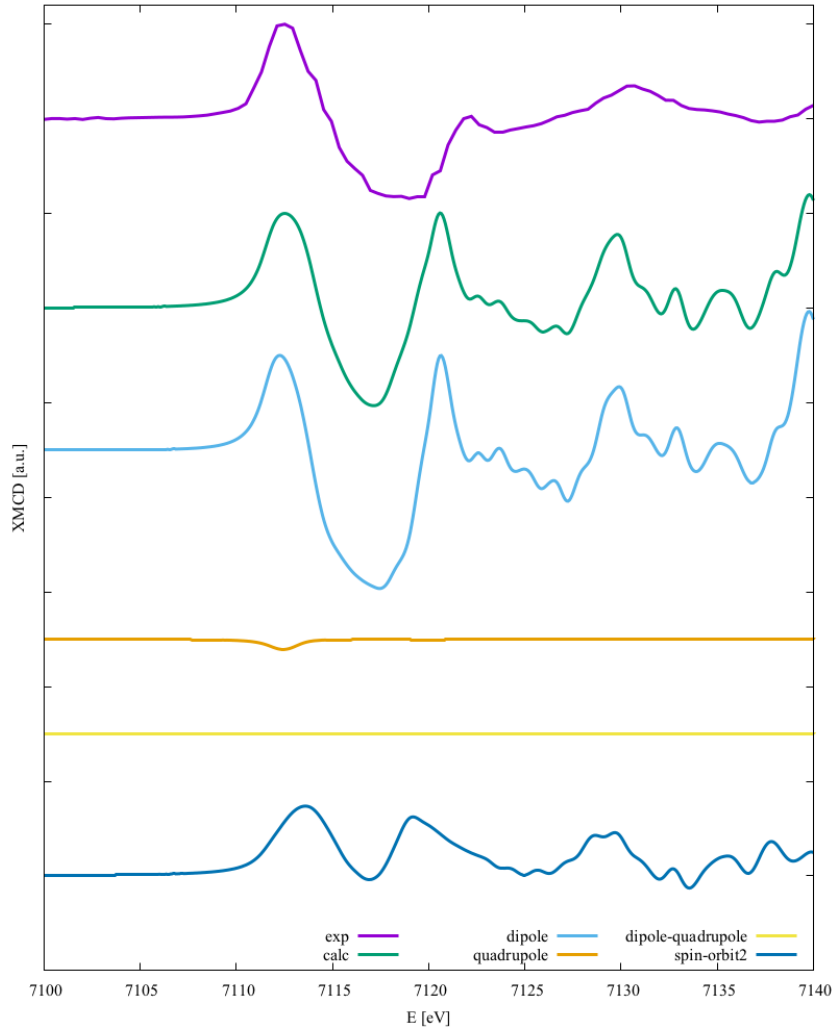


FIGURE 6.1: XMCD of bcc-Fe resolved into the different contributions. The experiment (purple) is taken from [126]. The overall shape is already reproduced with the dipole contribution, but the quotient between the first positive peak and the first negative peak can be improved when the σ_{D-SO2} is included. The quadrupole related terms have nearly zero influence on the spectrum.

application onto systems like those presented in Section 4.2, an explicit influence of the description of relativistic effects (scalar-relativistic or full-relativistic, i.e. with multicomponent spinors) will probably become important.

Bibliography

- [1] H. J. Farnsworth, *Futurama* **6**, 10 (2010).
- [2] G. E. Moore, *IEEE Solid-State Circuits Newsletter* **20**, 33 (2006).
- [3] M. Elbing, R. Ochs, M. Koentopp, *et al.*, *Proceedings of the National Academy of Sciences of the United States of America* **102**, 8815 (2005).
- [4] M. Fuechsle, J. A. Miwa, S. Mahapatra, *et al.*, *Nature Nanotechnology* **7**, 242 (2012).
- [5] R. Courtland and G. Moore, “Gordon Moore: The Man Whose Name Means Progress,” (2015).
- [6] R. Winkler and M. Oestreich, *Physik Journal* **3**, 39 (2004).
- [7] B. Grotz, M. V. Hauf, M. Dankerl, *et al.*, *Nature communications* **3**, 729 (2012).
- [8] M. Veldhorst, C. H. Yang, J. C. C. Hwang, *et al.*, *Nature* **526**, 410 (2015).
- [9] V. S. Denchev, S. Boixo, S. V. Isakov, *et al.*, *Physical Review X* **6**, 031015 (2016).
- [10] W. Gerlach and O. Stern, *Zeitschrift für Physik* **8**, 110 (1922).
- [11] W. Gerlach and O. Stern, *Zeitschrift für Physik* **9**, 353 (1922).
- [12] W. Gerlach and O. Stern, *Zeitschrift für Physik* **9**, 349 (1922).
- [13] S. Datta and B. Das, *Applied Physics Letters* **56**, 665 (1990).
- [14] S. Sasaki, K. Tateno, G. Zhang, *et al.*, *Applied Physics Letters* **103**, 213502 (2013).
- [15] J. M. Luttinger, *Journal of Mathematical Physics* **4**, 1154 (1963).

- [16] P. Giannozzi, S. Baroni, N. Bonini, *et al.*, Journal of Physics: Condensed Matter **21**, 395502 (2009).
- [17] R. M. Dreizler and E. K. U. Gross, *Density Functional Theory* (Springer Berlin Heidelberg, 1990).
- [18] L. Hoddeson, E. Braun, J. Teichmann, and S. Weart, eds., *Out of the crystal maze: A history of solid state physics* (Oxford University Press, USA, 1992).
- [19] H. Gummert, in *Studien zur Naturwissenschaft, Technik und Wirtschaft im 19. Jahrhundert* (Vandenhoeck and Ruprecht, Göttingen, 1976) p. 351.
- [20] H. Weber, Sitz. Preuss. Akad. **2**, 933 (1888).
- [21] M. Planck, Verhandlungen der Deutschen Physikalischen Gesellschaft **2**, 202 (1900).
- [22] M. Planck, Verhandlungen der Deutschen Physikalischen Gesellschaft **2**, 237 (1900).
- [23] J. J. Thomson, Philosophical Magazine Series 5 **44**, 293 (1897).
- [24] P. Drude, Annalen der Physik **306**, 566 (1900).
- [25] J. J. Thomson, in *Rapports présentés au Congrès international de physique III*, edited by C. É. Guillaume (Gauthier-Villars, Paris, 1900) p. 138.
- [26] H. A. Lorentz, in *Archives néerlandaises des sciences exactes et naturelles*, Vol. ser.2:t.10 (La Haye: Société hollandaise des sciences à Harlem, 1905) p. 336.
- [27] R. Franz and G. Wiedemann, Annalen der Physik und Chemie **165**, 497 (1853).
- [28] W. Friedrich, P. Knipping, and M. Laue, Annalen der Physik **346**, 971 (1913).
- [29] W. H. Bragg and W. L. Bragg, Proceedings of the Royal Society A: Mathematical, Physical and Engineering Sciences **88**, 428 (1913).
- [30] H. K. Onnes, Commun. Phys. Lab. Univ. Leiden **12**, 120 (1911).
- [31] A. Einstein, in *Albert Einstein: Philosopher-Scientist*, edited by P. A. Schilpp (The Library of Living Philosophers, Inc: Evanston, IL, 1949) 1st ed., p. 45.

-
- [32] A. Einstein, *Annalen der Physik* **322**, 132 (1905).
- [33] W. Heisenberg, *Physics and Philosophy* (Harper & Row Publishers, Inc., 1958).
- [34] N. Bohr, *Philosophical Magazine Series 6* **26**, 857 (1913).
- [35] L. De Broglie, *Ann. de Physique* **3**, 22 (1925).
- [36] W. Heisenberg, *Zeitschrift für Physik* **33**, 879 (1925).
- [37] M. Born and P. Jordan, *Zeitschrift für Physik* **34**, 858 (1925).
- [38] M. Born, W. Heisenberg, and P. Jordan, *Zeitschrift für Physik* **35**, 557 (1926).
- [39] E. Schrödinger, *Physical Review* **28**, 1049 (1926).
- [40] E. Schrödinger, *Annalen der Physik* **384**, 734 (1926).
- [41] C. Eckart, *Proceedings of the National Academy of Sciences* **12**, 473 (1926).
- [42] P. A. M. Dirac, *Physikalische Zeitschrift der Sowjetunion* **3**, 64 (1933).
- [43] P. Dirac, *Reviews of Modern Physics* **17**, 195 (1945).
- [44] R. P. Feynman, *Reviews of Modern Physics* **20**, 367 (1948).
- [45] P. Hohenberg and W. Kohn, *Physical Review* **136**, B864 (1964).
- [46] W. Kohn and L. J. Sham, *Physical Review* **140**, A1133 (1965).
- [47] F. Aryasetiawan and O. Gunnarsson, *Reports on Progress in Physics* **61**, 237 (1998), arXiv:9712013 [cond-mat] .
- [48] J. P. Perdew and M. Levy, *Physical Review Letters* **51**, 1884 (1983).
- [49] J. P. Perdew, K. Burke, and M. Ernzerhof, *Physical Review Letters* **77**, 3865 (1996).
- [50] A. Dal Corso and A. Mosca Conte, *Physical Review B* **71**, 115106 (2005).
- [51] L. L. Foldy and S. A. Wouthuysen, *Physical Review* **78**, 29 (1950).
- [52] J. D. Bjorken and S. D. Drell, *Relativistic Quantum Mechanics*, edited by L. I. Schiff (Mc Graw-Hill Book Company, New York, San Francisco, Toronto, London, 1964).
-

- [53] W. Kutzelnigg, *Chemical Physics* **225**, 203 (1997).
- [54] W. Liu and D. Peng, *The Journal of Chemical Physics* **131**, 031104 (2009).
- [55] R. J. Elliott, *Physical Review* **96**, 266 (1954).
- [56] E. van Lenthe, E. J. Baerends, and J. G. Snijders, *The Journal of Chemical Physics* **99**, 4597 (1993).
- [57] E. van Lenthe, J. G. Snijders, and E. J. Baerends, *The Journal of Chemical Physics* **105**, 6505 (1996).
- [58] P. Blöchl, *Physical Review B* **50**, 953 (1994).
- [59] U. Gerstmann, N. J. Vollmers, A. Lücke, M. Babilon, and W. G. Schmidt, *Physical Review B* **89**, 165431 (2014).
- [60] T. Hirahara, G. Bihlmayer, Y. Sakamoto, *et al.*, *Physical Review Letters* **107**, 166801 (2011).
- [61] Y. Koroteev, G. Bihlmayer, E. Chulkov, and S. Blügel, *Physical Review B* **77**, 045428 (2008).
- [62] C. L. Kane and E. J. Mele, *Physical Review Letters* **95**, 226801 (2005).
- [63] Y. Yao, F. Ye, X.-L. Qi, S.-C. Zhang, and Z. Fang, *Physical Review B* **75**, 041401 (2007).
- [64] J. C. Boettger and S. B. Trickey, *Physical Review B* **75**, 121402 (2007).
- [65] H. Bentmann, F. Forster, G. Bihlmayer, *et al.*, *EPL (Europhysics Letters)* **87**, 37003 (2009).
- [66] C. Ast, J. Henk, A. Ernst, *et al.*, *Physical Review Letters* **98**, 186807 (2007).
- [67] H. A. Kramers, *Proceedings Koninklijke Akademie van Wetenschappen* , 959 (1930).
- [68] G. Dresselhaus, *Phys.Rev.* **100**, 580 (1955).
- [69] E. I. Rashba, *Soviet Physics: Solid State* **1**, 368 (1959).
- [70] Y. A. Bychkov and E. I. Rashba, *Journal of Physics C* **17**, 6039 (1984).
- [71] F. Reich and T. Richter, *Journal für Praktische Chemie* **90**, 172 (1863).

- [72] F. Reich and T. Richter, *Journal für Praktische Chemie* **92**, 480 (1864).
- [73] A. G. Bhuiyan, A. Hashimoto, and A. Yamamoto, *Journal of Applied Physics* **94**, 2779 (2003).
- [74] A. Holleman, E. Wilberg, and N. Wilberg, *Lehrbuch der Anorganischen Chemie*, 102nd ed. (de Gruyter, 2007).
- [75] J. J. Lander and J. Morrison, *Journal of Applied Physics* **36**, 1706 (1965).
- [76] T. Abukawa, M. Sasaki, F. Hisamatsu, *et al.*, *Surface Science* **325**, 33 (1995).
- [77] I. Hill and a. McLean, *Physical Review B* **56**, 15725 (1997).
- [78] O. Bunk, G. Falkenberg, J. Zeysing, *et al.*, *Physical Review B* **59**, 12228 (1999).
- [79] H. Yeom, S. Takeda, E. Rotenberg, *et al.*, *Physical Review Letters* **82**, 4898 (1999).
- [80] T. Tanikawa, I. Matsuda, T. Kanagawa, and S. Hasegawa, *Physical Review Letters* **93**, 016801 (2004).
- [81] S. J. Park, H. W. Yeom, S. H. Min, D. H. Park, and I. W. Lyo, *Physical Review Letters* **93**, 1 (2004).
- [82] J. Guo, G. Lee, and E. W. Plummer, *Physical Review Letters* **95**, 2 (2005).
- [83] S. J. Park, H. W. Yeom, J. R. Ahn, and I. W. Lyo, *Physical Review Letters* **95**, 6 (2005).
- [84] C. González, J. Ortega, and F. Flores, *New Journal of Physics* **7** (2005), 10.1088/1367-2630/7/1/100.
- [85] C. González, F. Flores, and J. Ortega, *Physical Review Letters* **96**, 2 (2006).
- [86] J. Nitta, T. Akazaki, H. Takayanagi, and T. Enoki, *Physical Review Letters* **78**, 1335 (1997).
- [87] D. Grundler, *Physical Review Letters* **84**, 6074 (2000).
- [88] S. C. Erwin and F. J. Himpsel, *Nature communications* **1**, 58 (2010), arXiv:1008.5358 .

- [89] A. A. Stekolnikov, K. Seino, F. Bechstedt, *et al.*, Physical Review Letters **98**, 1 (2007).
- [90] H. J. Kim and J. H. Cho, Physical Review Letters **110**, 1 (2013).
- [91] I. Gierz, B. Stadtmüller, J. Vuorinen, *et al.*, Physical Review B **81**, 245430 (2010).
- [92] D. Popović, F. Reinert, S. Hübner, *et al.*, Physical Review B **72**, 045419 (2005).
- [93] S. LaShell, B. McDougall, and E. Jensen, Physical Review Letters **77**, 3419 (1996).
- [94] H. Cercellier, C. Didiot, Y. Fagot-Revurat, *et al.*, Physical Review B **73**, 195413 (2006).
- [95] Y. Koroteev, G. Bihlmayer, J. Gayone, *et al.*, Physical Review Letters **93**, 046403 (2004).
- [96] Z. Yu, Y. X. Huang, and S. C. Shen, Physical Review B **39**, 6287 (1989).
- [97] C.-F. Geoffroy, in *Histoire de l'Académie royale des sciences*, edited by J. Boudot (Imprimerie royale, Paris, 1753) Chap. Mémoires, pp. 296–312.
- [98] H. G. de Carvalho and M. de Araújo Penna, Lettere al Nuovo Cimento **3**, 720 (1972).
- [99] P. de Marcillac, N. Coron, G. Dambier, J. Leblanc, and J.-P. Moalic, Nature **422**, 876 (2003).
- [100] T. Hirahara, K. Miyamoto, I. Matsuda, *et al.*, Physical Review B - Condensed Matter and Materials Physics **76**, 1 (2007).
- [101] I. K. Drozdov, A. Alexandradinata, S. Jeon, *et al.*, Nature Physics **10**, 664 (2014), arXiv:1404.2598 .
- [102] T. Hirahara, I. Matsuda, S. Yamazaki, *et al.*, Applied Physics Letters **91**, 1 (2007).
- [103] G. Jnawali, C. Klein, T. Wagner, *et al.*, Physical Review Letters **108**, 1 (2012).

-
- [104] X. Gonze, J.-P. Michenaud, and J.-P. Vigneron, *Physical Review B* **41**, 11827 (1990).
- [105] P. Hofmann, *Progress in Surface Science* **81**, 191 (2006).
- [106] C. Klein, *Erzeugung, Analyse und Manipulation von Systemen mit spin-aufgespaltenen Zuständen*, Ph.D. thesis, Universität Duisburg-Essen (2015).
- [107] D. Schiferl and C. S. Barrett, *Journal of Applied Crystallography* **2**, 30 (1969).
- [108] H. Mönig, J. Sun, Y. M. Koroteev, *et al.*, *Physical Review B* **72**, 085410 (2005).
- [109] H. Du, X. Sun, X. Liu, *et al.*, *Nature Communications* **7**, 10814 (2016).
- [110] T. Hirahara, T. Nagao, I. Matsuda, *et al.*, *Physical Review Letters* **97**, 10 (2006).
- [111] Y. Ohtsubo, L. Perfetti, M. O. Goerbig, *et al.*, *New Journal of Physics* **15**, 033041 (2013).
- [112] M. C. Cottin, C. A. Bobisch, J. Schaffert, *et al.*, *Applied Physics Letters* **98**, 022108 (2011).
- [113] A. Takayama, T. Sato, S. Souma, and T. Takahashi, *New Journal of Physics* **16**, 055004 (2014).
- [114] C. R. Ast and H. Höchst, *Physical Review B* **66**, 125103 (2002).
- [115] C. R. Ast and H. Höchst, *Physical Review Letters* **90**, 016403 (2003).
- [116] D. Lükermann, S. Sologub, H. Pfnür, *et al.*, *Physical Review B* **86**, 195432 (2012).
- [117] P. Kröger, S. Sologub, C. Tegenkamp, and H. Pfnür, *Journal of Physics: Condensed Matter* **26**, 225002 (2014).
- [118] T. Schlenk, M. Bianchi, M. Koleini, *et al.*, *Physical Review Letters* **110**, 126804 (2013).
- [119] D. West, Y. Y. Sun, S. B. Zhang, *et al.*, *Physical Review B* **85**, 081305 (2012).

- [120] C.-L. Song, Y.-P. Jiang, Y.-L. Wang, *et al.*, Physical Review B **86**, 045441 (2012).
- [121] C. Klein, N. J. Vollmers, U. Gerstmann, *et al.*, Physical Review B **91**, 195441 (2015).
- [122] N. J. Vollmers, C. Klein, M. Horn-Von Hoegen, *et al.*, to be submitted (2016).
- [123] G. Henkelman and H. Jonsson, The Journal of Chemical Physics **113**, 9978 (2000).
- [124] M. F. Chisholm, S. J. Pennycook, R. Jebasinski, and S. Mantl, Applied Physics Letters **64**, 2409 (1994).
- [125] M. Taillefumier, D. Cabaret, A.-M. Flank, and F. Mauri, Physical Review B **66**, 195107 (2002).
- [126] O. Mathon, F. Baudelet, J.-P. Itié, *et al.*, Journal of Synchrotron Radiation **11**, 423 (2004).
- [127] C. Gougoussis, *Excitations électroniques et magnétisme des matériaux : calcul ab initio de l'absorption X et du dichroïsme circulaire magnétique au seuil K*, Ph.D. thesis, Université Pierre et Marie Curie (2009).
- [128] R. Wu and A. J. Freeman, Physical Review Letters **73**, 1994 (1994).
- [129] J. Stöhr and H. König, Physical Review Letters **75**, 3748 (1995).
- [130] M. Komelj, C. Ederer, J. W. Davenport, and M. Fähnle, Physical Review B **66**, 140407 (2002).
- [131] T. Oguchi and T. Shishidou, Physical Review B **70**, 024412 (2004).